

An Edge-Based Smoothed Finite Element Method with TBC for the Elastic Wave Scattering by an Obstacle

Ze Wu¹, Junhong Yue^{2,*}, Ming Li^{2,*}, Ruiping Niu¹, Yufei Zhang²

¹ College of Mathematics, Taiyuan University of Technology, 030024, Taiyuan, China.

² College of Data Science, Taiyuan University of Technology, 030024, Taiyuan, China.

Received 29 May 2020; Accepted (in revised version) 24 December 2020

Abstract. Elastic wave scattering has received ever-increasing attention in military and medical fields due to its high-precision solution. In this paper, an edge-based smoothed finite element method (ES-FEM) combined with the transparent boundary condition (TBC) is proposed to solve the elastic wave scattering problem by a rigid obstacle with smooth surface, which is embedded in an isotropic and homogeneous elastic medium in two dimensions. The elastic wave scattering problem satisfies Helmholtz equations with coupled boundary conditions obtained by Helmholtz decomposition. Firstly, the TBC of the elastic wave scattering is constructed by using the analytical solution to Helmholtz equations, which can truncate the boundary value problem (BVP) in an unbounded domain into the BVP in a bounded domain. Then the formulations of ES-FEM with the TBC are derived for Helmholtz equations with coupled boundary conditions. Finally, several numerical examples illustrate that the proposed ES-FEM with the TBC (ES-FEM-TBC) can work effectively and obtain more stable and accurate solution than the standard FEM with the TBC (FEM-TBC) for the elastic wave scattering problem.

AMS subject classifications: 35Q99, 65N99

Key words: Elastic wave scattering problem, edge-based smoothed finite element method, Helmholtz equations, transparent boundary condition.

1 Introduction

The obstacle scattering is a basis issue of scattering theory, which considers the incident wave scattering by an impenetrable and bounded media. It plays an increasingly important role in many scientific and engineering fields, such as target detection and positioning in radar and sonar; imaging of single proteins in medical imaging and oil and gas

*Corresponding author. *Email addresses:* 1395169950@qq.com (Z. Wu), woyuejunhong@163.com (J. Yue), liming01@tyut.edu.cn (M. Li), niu_ruiping2007@126.com (R. Niu), zhangyufeiting@foxmail.com (Y. Zhang)

exploration in geophysical exploration [1]. Common scattering problem mainly include: acoustic scattering, elastic wave scattering and electromagnetic wave scattering. Compare to acoustic and electromagnetic wave scattering [2–4], the elastic wave scattering is less studied because of the existence of compressional and shear waves, which will increase computational difficulty. However, because the elastic wave scattering can obtain more accurate solution, it has recently attracted more and more attention in geophysics and seismology [5–10]. Meanwhile, the existence and uniqueness for solution to the elastic scattering problem have been demonstrated in Refs. [11, 12]. The analytical solution has been usually obtained for the wave scattering with simple geometrical obstacle [13], while it is difficult to obtain the analytical solution for obstacles with relatively complicated shapes.

Therefore, to tackle the wave scattering problem by more complicate obstacle, some numerical methods have been proposed for solving direct and inverse obstacle scattering [2,14], such as finite element method (FEM) [3,15–17], boundary integral method [18] and dynamical functional particle method (DFPM) [19]. Among these numerical methods, the FEM is a widely used and powerful numerical method. Considering that the elastic wave scattering is described as an exterior boundary value problem imposed in an unbounded domain, people usually truncate the unbounded domain into a bounded domain before using the FEM solves the problem. There are two common truncation techniques: one is the transparent boundary condition (TBC), the other is a technique called the perfectly matched layer (PML). The TBC was firstly proposed based on a non-local Dirichlet-to-Neumann (DtN) operator, which is defined by an infinite Fourier series. By imposing the TBC on the boundary of the truncated domain, the artificial wave reflection can not occur. The TBC has been applied to work out some wave scattering problems [2, 14, 20–24]. The PML technique was proposed by Berenger [25], which uses an artificial layer to truncate the computational region. The layer can guarantee that the scattered wave is not reflected from the PML medium. The application of the PML can be founded in researches [3,26–28].

Though the FEM combined with the TBC or PML can handle the elastic wave scattering problem, the accuracy of the solution is not particularly high due to over-stiff characteristic of the FEM. To avoid over-stiff drawback and improve the accuracy of the solution, Liu et al. established the G space theory and proposed the weakened weak (W2) formulations [29–31] for some numerical methods, e.g. smoothed finite element method (S-FEM) [32–36] and smoothed point interpolation method (S-PIM) [37–39]. The S-FEM can soften over-stiff behavior of the FEM, hence the method has been extensively employed in various problem, such as wave problem [40–46], contact problem [47, 48], solid mechanics problem [12, 49–51] and fracture problem [53, 54]. In general, the S-FEM model can be classified into different smoothed finite element models based on different types of the smoothing domain. There are four common models, which are a cell-based smoothed finite element method (CS-FEM), a node-based smoothed finite element method (NS-FEM), an edge-based smoothed finite element method (ES-FEM) and a face-based smoothed finite element method (FS-FEM). In these common models, the ES-FEM

is a more effective numerical model. The ES-FEM has been proved to have many excellent properties, e.g. spatial discrete stability, time response stability and possessing near-accurate stiffness and so on. Especially, it has been also demonstrated that the ES-FEM can control effectively the pollution error and enhance the accuracy of the solution to the acoustic scattering problem [40, 42]. Because the result of the ES-FEM for acoustic scattering is superior clearly to the standard FEM, we hope that the ES-FEM can still deal with efficiently the elastic wave scattering.

In this paper, we consider the ES-FEM with the TBC to handle the elastic wave scattering problem by the obstacle with smooth surface. The elastic wave scattering problem is described through the Navier equations and Helmholtz equations with coupled boundary conditions in Section 2. The FEM formulations with the TBC are provided for Helmholtz equations with coupled boundary conditions in Section 3. The detailed formulations of the ES-FEM-TBC are derived for Helmholtz equations with coupled boundary conditions in Section 4. Several typical numerical examples are studied and discussed in Section 5. Some relevant conclusions and directions for future research are concluded in Section 6.

2 Problem statement

In this paper, we consider a time-harmonic plane elastic wave scattering problem in an isotropic homogeneous elastic medium by rigid obstacle D with arbitrarily smooth surface, whose boundary is Γ_D . The infinite area outside the obstacle is represented by Ω , as shown in Fig. 1.

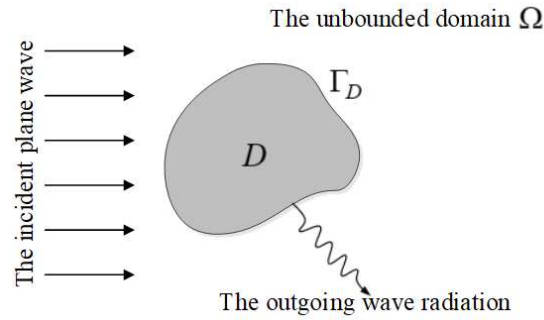


Figure 1: Geometry of an obstacle with arbitrary shape resulting in scattering of a time-harmonic plane elastic wave.

2.1 The Navier equation for the elastic wave scattering

Given an incident plane elastic wave \mathbf{u}^{inc} by obstacle, we have the Navier equation:

$$\mu\Delta\mathbf{u}^{inc} + (\lambda + \mu)\nabla\nabla\cdot\mathbf{u}^{inc} + \omega^2\mathbf{u}^{inc} = 0 \quad \text{in } \Omega, \quad (2.1)$$

where $\omega > 0$ is the angular frequency and λ, μ are the Lamé constants, satisfying $\mu > 0, \lambda + \mu > 0$.

The incident field $\mathbf{u}^{inc} = (u_1^{inc}, u_2^{inc})$ can take the following forms:

$$\begin{cases} \mathbf{u}_p^{inc} = \mathbf{d} e^{i\kappa_p \mathbf{x} \cdot \mathbf{d}}, & \text{for a compressional plane wave,} \\ \mathbf{u}_s^{inc} = \mathbf{d}^\perp e^{i\kappa_s \mathbf{x} \cdot \mathbf{d}}, & \text{for a shear plane wave,} \end{cases} \quad (2.2)$$

where $\mathbf{d} = (\cos\theta, \sin\theta)^T$ and $\mathbf{d}^\perp = (-\sin\theta, \cos\theta)^T$ are orthogonal vectors; $\theta \in [0, 2\pi]$ is an incident angle; κ_p and κ_s represent the compressional and shear wavenumbers, respectively, and can be given as follows:

$$\kappa_p = \omega / \sqrt{\lambda + 2\mu}, \quad \kappa_s = \omega / \sqrt{\mu}. \quad (2.3)$$

Similarly, we also have the Navier equation for the total wave field $\mathbf{u} = (u_1, u_2)$:

$$\mu \Delta \mathbf{u} + (\lambda + \mu) \nabla \nabla \cdot \mathbf{u} + \omega^2 \mathbf{u} = 0 \quad \text{in } \Omega. \quad (2.4)$$

Since the obstacle is rigid elastically, the total field \mathbf{u} satisfies the following boundary condition:

$$\mathbf{u} = 0 \quad \text{on } \Gamma_D. \quad (2.5)$$

The total field \mathbf{u} can be written as

$$\mathbf{u} = \mathbf{u}^{inc} + \mathbf{v}, \quad (2.6)$$

where \mathbf{v} is the scattered field, which is a vector with two components v_1 and v_2 , i.e. $\mathbf{v} = (v_1, v_2)$.

Subtracting Eq. (2.1) from Eq. (2.4) yields

$$\mu \Delta \mathbf{v} + (\lambda + \mu) \nabla \nabla \cdot \mathbf{v} + \omega^2 \mathbf{v} = 0 \quad \text{in } \Omega, \quad (2.7)$$

and the Dirichlet boundary condition on Γ_D ,

$$\mathbf{v} = -\mathbf{u}^{inc} \quad \text{on } \Gamma_D. \quad (2.8)$$

In addition, the scattered wave \mathbf{v} is required to satisfy the Kupradze radiation conditions on the far field:

$$\begin{cases} \hat{\mathbf{x}} \cdot \nabla \nabla \cdot \mathbf{v} - i\kappa_p \nabla \cdot \mathbf{v} = o\left(\frac{1}{|x|}\right), & |x| \rightarrow \infty, \\ \hat{\mathbf{x}} \cdot \nabla \mathbf{curl} \mathbf{v} - i\kappa_s \mathbf{curl} \mathbf{v} = o\left(\frac{1}{|x|}\right), & |x| \rightarrow \infty, \end{cases} \quad (2.9)$$

where $\hat{\mathbf{x}} = \mathbf{x} / |\mathbf{x}|$.

2.2 Helmholtz equations with coupled boundary conditions

For the solution v to Navier equation, the Helmholtz decomposition can be expressed by:

$$v = \nabla\phi + \mathit{curl}\psi, \quad (2.10)$$

where ϕ and ψ are scalar potential functions, which are called Lamé potentials, and $\mathit{curl}\psi = [\partial_y\psi \ -\partial_x\psi]^T$.

Substituting Eq. (2.10) into Navier Eq. (2.7) yields

$$\nabla[(\lambda+2\mu)(\Delta\phi) + \omega^2\phi] + \mathit{curl}[\mu\Delta\psi + \omega^2\psi] = 0, \quad (2.11)$$

which is satisfied, if ϕ and ψ satisfy the Helmholtz equations

$$\Delta\phi + \kappa_p^2\phi = 0, \quad \Delta\psi + \kappa_s^2\psi = 0 \quad \text{in } \Omega, \quad (2.12)$$

where κ_p and κ_s are wavenumbers defined in Eq. (2.3).

On the far field, the ϕ and ψ satisfy the Sommerfeld radiation conditions

$$\lim_{\rho \rightarrow +\infty} \rho^{1/2}(\partial_\rho\phi - i\kappa_p\phi) = 0, \quad \lim_{\rho \rightarrow +\infty} \rho^{1/2}(\partial_\rho\psi - i\kappa_s\psi) = 0, \quad \rho = |\mathbf{x}|, \quad \rho \in \Omega. \quad (2.13)$$

By the Helmholtz decomposition, the boundary condition defined in Eq. (2.8) can be rewritten as

$$\partial_\nu\phi + \partial_\tau\psi = u, \quad \partial_\nu\psi - \partial_\tau\phi = v \quad \text{on } \Gamma_D, \quad (2.14)$$

where $u = -\nu \cdot \mathbf{u}^{inc}$, $v = \boldsymbol{\tau} \cdot \mathbf{u}^{inc}$, in which $\nu = (\nu_1, \nu_2)^T$ and $\boldsymbol{\tau} = (\tau_1, \tau_2)^T$ are the unit normal and tangential vectors on vector of boundary Γ_D , and $\tau_1 = -\nu_2$, $\tau_2 = \nu_1$.

3 Finite element formulation with TBC

3.1 TBC formulation

Since the standard FEM model can not solve directly the elastic wave scattering problem in open region, the unbounded domain needs to be truncated into a bounded computational domain. In this paper, the TBC is imposed on the boundary of truncated domain, which is called the transparent boundary Γ_B , as shown in Fig. 2.

From Fig. 2, it can be seen that the original infinite region Ω is divided into two parts by the transparent boundary Γ_B : the bounded domain Ω_i and the unbounded domain Ω_o , i.e. $\Omega = \Omega_i + \Omega_o$. Hence, the boundary of the bounded domain is composed of Γ_B and Γ_D .

Moreover, this problem is usually regarded as an external boundary value problem in Ω_o and solved analytically. However, in order to get the analytical solution easily and quickly, the geometry of Γ_B is usually as simple as possible. For example, a simple sphere is applied to 3D problem, or a circle is applied to 2D problem.

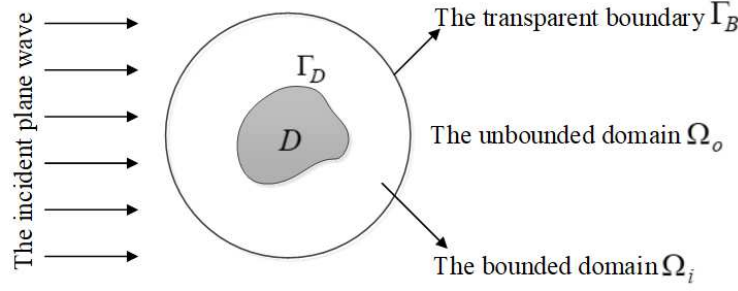


Figure 2: Geometry of obstacle scattering problem domain with the transparent boundary Γ_B .

Next, we will illustrate how to obtain the DtN operator on Γ_B .

Firstly, we can know the following relationships on Γ_B :

$$\frac{\partial \phi}{\partial n} = -\mathcal{M}_1 \phi, \quad \frac{\partial \psi}{\partial n} = -\mathcal{M}_2 \psi, \quad \text{on } \Gamma_B, \quad (3.1)$$

where $\mathcal{M}_1, \mathcal{M}_2$ are the DtN operator and $\frac{\partial \phi}{\partial n}, \frac{\partial \psi}{\partial n}$ are normal derivative of ϕ, ψ on Γ_B , respectively.

Observing Eq. (3.1), it can be found that if ϕ, ψ and their normal derivative are known, the expression of the DtN operator can be obtained. The analytical solutions (ϕ, ψ) to the exterior boundary value problem in Ω_o can be expressed by:

$$\phi(r, \theta) = \frac{1}{\pi} \sum_{n=0}^{\prime} \int_0^{2\pi} \frac{H_n^{(1)}(\kappa_p r)}{H_n^{(1)}(\kappa_p R)} \cos n(\theta - \theta') \phi(R, \theta') d\theta', \quad (3.2)$$

$$\psi(r, \theta) = \frac{1}{\pi} \sum_{n=0}^{\prime} \int_0^{2\pi} \frac{H_n^{(1)}(\kappa_s r)}{H_n^{(1)}(\kappa_s R)} \cos n(\theta - \theta') \psi(R, \theta') d\theta', \quad (3.3)$$

where R is the radius of Γ_B , $\phi(R, \theta')$ and $\psi(R, \theta')$ are given Dirichlet data on Γ_B . $H_n^{(1)}$ is the Hankel function of the first kind with n order, and the prime after the sum means that the corresponding value is halved for the first term.

By differentiating Eqs. (3.2)-(3.3) with respect to r , respectively, we have

$$\phi_v = \frac{\partial \phi(r, \theta)}{\partial n} \Big|_{r=R} = - \sum_{n=0}^{\prime} \int_0^{2\pi} m_1(\theta - \theta') \phi(R, \theta') d\theta', \quad (3.4)$$

$$\psi_v = \frac{\partial \psi(r, \theta)}{\partial n} \Big|_{r=R} = - \sum_{n=0}^{\prime} \int_0^{2\pi} m_2(\theta - \theta') \psi(R, \theta') d\theta', \quad (3.5)$$

where coefficients $m_1(\theta - \theta')$, $m_2(\theta - \theta')$ are expressed by

$$m_1(\theta - \theta') = -\frac{\kappa_p H_n^{(1)'(\kappa_p R)}}{\pi H_n^{(1)}(\kappa_p R)} (\cos n\theta \cos n\theta' + \sin n\theta \sin n\theta'), \quad (3.6)$$

$$m_2(\theta - \theta') = -\frac{\kappa_s H_n^{(1)'(\kappa_s R)}}{\pi H_n^{(1)}(\kappa_s R)} (\cos n\theta \cos n\theta' + \sin n\theta \sin n\theta'). \quad (3.7)$$

Finally, the DtN operator can be obtained by substituting Eqs. (3.2)-(3.3) and Eqs. (3.4)-(3.5) into Eq. (3.1).

3.2 FEM formulation for Helmholtz equations with coupled boundary conditions

In the subsection, the standard Galerkin weak forms of Helmholtz equations with coupled boundary conditions with the TBC are derived in detail based on the DtN operator. Through the Scalar Green's theorem of the second kind, we have:

$$\begin{cases} \int_{\Omega_i} \nabla \zeta \nabla \phi d\Omega - \kappa_p^2 \int_{\Omega_i} \zeta \phi d\Omega + \int_{\Gamma_B} \zeta \mathcal{M}_1 \phi d\Gamma + \int_{\Gamma_D} \zeta \partial_\tau \psi d\Gamma = \int_{\Gamma_D} \zeta u d\Gamma, \\ \int_{\Omega_i} \nabla \eta \nabla \psi d\Omega - \kappa_s^2 \int_{\Omega_i} \eta \psi d\Omega + \int_{\Gamma_B} \eta \mathcal{M}_2 \psi d\Gamma - \int_{\Gamma_D} \eta \partial_\tau \phi d\Gamma = \int_{\Gamma_D} \eta v d\Gamma, \end{cases} \quad (3.8)$$

where ζ and η are test functions, corresponding to potential functions ϕ and ψ , respectively.

Assuming that the solution to the elastic wave scattering problem can be approximated in terms of the following form:

$$\phi = \sum N_i \phi_i = \mathbf{N} \boldsymbol{\phi}, \quad \psi = \sum N_i \psi_i = \mathbf{N} \boldsymbol{\psi}, \quad (3.9)$$

where ϕ_i and ψ_i are the value of ϕ and ψ at node i , respectively, and N_i is the FEM shape function at node i .

By substituting Eq. (3.9) into Eq. (3.8), the discrete formulation of Eq. (3.8) can be written as

$$[\mathbf{K} - \mathbf{P} + \mathbf{K}_{AB} + \mathbf{K}_b] \boldsymbol{\Phi} = \mathbf{F}, \quad (3.10)$$

where $\boldsymbol{\Phi}$ is an unknown nodal vector, i.e. $\boldsymbol{\Phi} = [\boldsymbol{\phi} \ \boldsymbol{\psi}]^T$, in which $\boldsymbol{\phi}$ and $\boldsymbol{\psi}$ consist of $\boldsymbol{\phi}^e$ and $\boldsymbol{\psi}^e$, respectively.

The system stiffness matrix \mathbf{K} consists of element stiffness matrix \mathbf{K}^e , and

$$\mathbf{K}^e = \begin{bmatrix} \mathbf{K}_1^e & 0 \\ 0 & \mathbf{K}_2^e \end{bmatrix}, \quad (3.11)$$

with $\mathbf{K}_1^e = \mathbf{K}_2^e = \int_{\Omega_e} \mathbf{B}^{eT} \mathbf{B}^e d\Omega$, where Ω_e is the element mesh in the computational domain.

The mass matrix \mathbf{P} consists of element mass matrix \mathbf{P}^e , and

$$\mathbf{P}^e = \begin{bmatrix} \kappa_p^2 \mathbf{P}_1^e & 0 \\ 0 & \kappa_s^2 \mathbf{P}_2^e \end{bmatrix}, \quad (3.12)$$

with $\mathbf{P}_1^e = \mathbf{P}_2^e = \int_{\Omega_e} \mathbf{N}^T \mathbf{N} d\Omega$. And the obstacle boundary stiffness matrix \mathbf{K}_b can be calculated using

$$\mathbf{K}_b = \begin{bmatrix} 0 & b_1^e \\ -b_1^e & 0 \end{bmatrix}, \quad (3.13)$$

and the \mathbf{K}_{AB} denotes the matrix which is associated with the DtN map and can be given by

$$\mathbf{K}_{AB} = \begin{bmatrix} \mathbf{K}_{AB}^1 & 0 \\ 0 & \mathbf{K}_{AB}^2 \end{bmatrix}, \quad (3.14)$$

where the element of the matrix $\mathbf{K}_{AB}^1, \mathbf{K}_{AB}^2$ on row i , column j can be given by $\mathbf{K}_{IJ}^1, \mathbf{K}_{IJ}^2$, respectively. The \mathbf{K}_{IJ}^1 and \mathbf{K}_{IJ}^2 can be expressed as:

$$\begin{aligned} \mathbf{K}_{IJ}^1 &= \int_{\Gamma_B} \mathbf{N}_I \mathbf{M}_1 \mathbf{N}_J d\Gamma \\ &= - \sum_{j=0}^{\infty} \frac{\kappa_p}{\pi} \frac{H_n^{(1)'(\kappa_p R)}}{H_n^{(1)}(\kappa_p R)} \left(\int_{\Gamma_B} \mathbf{N}_I(\mathbf{x}) F_j(\mathbf{x}) d\Gamma \right) \times \left(\int_{\Gamma_B} \mathbf{N}_J(\mathbf{x}) F_j(\mathbf{x}') d\Gamma \right), \end{aligned} \quad (3.15)$$

$$\begin{aligned} \mathbf{K}_{IJ}^2 &= \int_{\Gamma_B} \mathbf{N}_I \mathbf{M}_2 \mathbf{N}_J d\Gamma \\ &= - \sum_{j=0}^{\infty} \frac{\kappa_s}{\pi} \frac{H_n^{(1)'(\kappa_s R)}}{H_n^{(1)}(\kappa_s R)} \left(\int_{\Gamma_B} \mathbf{N}_I(\mathbf{x}) F_j(\mathbf{x}) d\Gamma \right) \times \left(\int_{\Gamma_B} \mathbf{N}_J(\mathbf{x}) F_j(\mathbf{x}') d\Gamma \right), \end{aligned} \quad (3.16)$$

in which \mathbf{N}_I and \mathbf{N}_J denote the corresponding shape functions associated with node i and j , the functions $F_j(\mathbf{x})$ and $F_j(\mathbf{x}')$ are given by

$$F_j(\mathbf{x}) = [\cos n\theta \quad \sin n\theta], \quad F_j(\mathbf{x}') = [\cos n\theta' \quad \sin n\theta'], \quad (3.17)$$

and the obstacle boundary element force vector can be calculated using

$$\mathbf{F}^e = [\mathbf{F}_1^e \quad \mathbf{F}_2^e]^T, \quad (3.18)$$

with $\mathbf{F}_1^e = \int_{\Gamma_D^e} \mathbf{N}^T u d\Gamma, \mathbf{F}_2^e = \int_{\Gamma_D^e} \mathbf{N}^T v d\Gamma$.

4 Formulation of S-FEM with TBC

The S-FEM is a numerical method using the weakened weak formulation, which uses a kind of smoothing operation to approximate the derivative of function $w_l(\mathbf{x})$ with respect to x_i . The formulation can be given:

$$\overline{\frac{\partial w_l}{\partial x_i}}(\mathbf{x}) = \frac{1}{A_s} \int_{\Gamma_s} w_l(s) n_i ds, \quad i = 1, \dots, d, \quad \forall \mathbf{x} \in \Omega_s, \quad (4.1)$$

where $w_l(\mathbf{x})$ is the l th component of function $w(\mathbf{x})$, $\mathbf{x} = (x_1, x_2, \dots, x_d)$, in which d is the dimension of smoothing domain Ω_s . A_s is the area of Ω_s and Γ_s is the boundary of Ω_s . Hence, the gradient or derivative of any function is approximated by the Gauss quadrature along the boundary of the smoothing domain as Eq. (4.1). The 2D problem usually adopt a Gauss-point.

4.1 Edge-based smoothing domains

The construction of edge-based smoothing domains (E-SDs) is introduced in this section. For a triangular element, the construction of the E-SDs is accomplished by connecting the two endpoints of the edge with the centroid of the adjacent two elements. In this paper, the number of smoothing domain is the same as the number of edge in the mesh. Fig. 3 shows the ES-FEM model using triangular elements with the solid line, the smoothing domain $\Omega_{k_i}^s$ for interior edge k_i , or $\Omega_{k_b}^s$ for boundary edge k_b , which is the shade domain with dash line, and $\Gamma_{k_i}^s, \Gamma_{k_b}^s$ corresponding to the boundary of $\Omega_{k_i}^s, \Omega_{k_b}^s$, respectively.

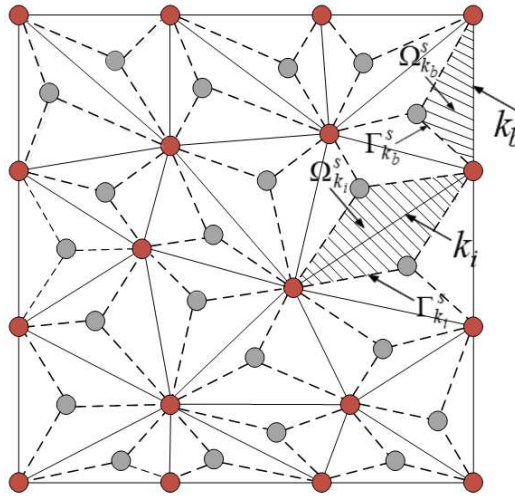


Figure 3: The background mesh using triangular elements with the solid line, and the smoothing domain $\Omega_{k_i}^s$ for interior edge k_i , or $\Omega_{k_b}^s$ for boundary edge k_b , which is the shade domain with dash line, and $\Gamma_{k_i}^s, \Gamma_{k_b}^s$ corresponding to the boundary of $\Omega_{k_i}^s, \Omega_{k_b}^s$, respectively.

4.2 Weakened weak form for Helmholtz equations with coupled boundary conditions

The weakened weak form for Helmholtz equations with coupled boundary conditions is derived in this part. Based on the smoothing operator, the weakened weak forms of

Eq. (3.8) on the smoothing domains are expressed by:

$$\begin{cases} \sum_{i=1}^{N_s} \int_{\Omega_s} \nabla \bar{\phi} \cdot \nabla \bar{\xi} d\Omega - \kappa_p^2 \int_{\Omega_i} \phi \bar{\xi} d\Omega + \int_{\Gamma_B} \bar{\xi} \mathcal{M}_1 \phi d\Gamma + \int_{\Gamma_D} \bar{\xi} \partial_\tau \psi d\Gamma = \int_{\Gamma_D} \bar{\xi} u d\Gamma, \\ \sum_{i=1}^{N_s} \int_{\Omega_s} \nabla \bar{\psi} \cdot \nabla \bar{\eta} d\Omega - \kappa_s^2 \int_{\Omega_i} \eta \bar{\psi} d\Omega + \int_{\Gamma_B} \bar{\eta} \mathcal{M}_2 \psi d\Gamma - \int_{\Gamma_D} \bar{\eta} \partial_\tau \phi d\Gamma = \int_{\Gamma_D} \bar{\eta} v d\Gamma, \end{cases} \quad (4.2)$$

where N_s is the number of the E-SDs, and the smoothed gradients are discretized through the following forms:

$$\begin{aligned} \nabla \bar{\phi} &= \frac{1}{A_s} \int_{\Omega_s} \nabla \phi d\Omega = \frac{1}{A_s} \int_{\Gamma_s} N(\mathbf{x}) \mathbf{n}(\mathbf{x}) d\Gamma \boldsymbol{\phi} = \bar{\mathbf{B}} \boldsymbol{\phi}, \\ \nabla \bar{\psi} &= \frac{1}{A_s} \int_{\Omega_s} \nabla \psi d\Omega = \frac{1}{A_s} \int_{\Gamma_s} N(\mathbf{x}) \mathbf{n}(\mathbf{x}) d\Gamma \boldsymbol{\psi} = \bar{\mathbf{B}} \boldsymbol{\psi}, \end{aligned} \quad (4.3)$$

and

$$\begin{aligned} \bar{\mathbf{B}} &= [\bar{\mathbf{B}}_1 \ \bar{\mathbf{B}}_2 \ \cdots \ \bar{\mathbf{B}}_N]; \quad \bar{\mathbf{B}}_I = [\bar{\mathbf{B}}_{Ix} \ \bar{\mathbf{B}}_{Iy}]^T, \\ \boldsymbol{\phi} &= [\phi_1 \ \phi_2 \ \cdots \ \phi_N]^T; \quad \boldsymbol{\psi} = [\psi_1 \ \psi_2 \ \cdots \ \psi_N]^T. \end{aligned} \quad (4.4)$$

Substituting Eq. (4.3) into Eq. (4.2), we obtain:

$$[\bar{\mathbf{K}} - \mathbf{P} + \mathbf{K}_{AB} + \mathbf{K}_b] \boldsymbol{\Phi} = \mathbf{F}, \quad (4.5)$$

where $\boldsymbol{\Phi}$ is an unknown nodal vector, i.e. $\boldsymbol{\Phi} = [\boldsymbol{\phi} \ \boldsymbol{\psi}]^T$.

The system stiffness matrix $\bar{\mathbf{K}}$ is expressed by:

$$\bar{\mathbf{K}} = \begin{bmatrix} \bar{\mathbf{K}}_1 & 0 \\ 0 & \bar{\mathbf{K}}_2 \end{bmatrix}, \quad (4.6)$$

with $\bar{\mathbf{K}}_1 = \bar{\mathbf{K}}_2 = \sum_{i=1}^{N_s} \int_{\Omega_s} \bar{\mathbf{B}}^T \bar{\mathbf{B}} d\Omega$.

5 Numerical experiments

In this section, several numerical examples are presented to test the accuracy and efficiency of the ES-FEM-T3-TBC for the elastic wave scattering problem. These numerical experiments can be implemented by MATLAB in this paper. In order to estimate the error of the numerical approximation, the relative error is defined by

$$\mathbf{E}_\eta = \sqrt{\frac{\sum_{i=1}^N (\bar{\mathbf{v}}_i^e - \bar{\mathbf{v}}_i^n)^T (\mathbf{v}_i^e - \mathbf{v}_i^n)}{\sum_{i=1}^N (\bar{\mathbf{v}}_i^e)^T (\mathbf{v}_i^e)}}, \quad (5.1)$$

where \mathbf{v}_i^e and \mathbf{v}_i^n are analytical/reference solution and numerical solution; $\bar{\mathbf{v}}_i^e$ and $\bar{\mathbf{v}}_i^n$ are their complex conjugates, respectively; N is the number of nodes considered.

It is known that the numerical error will become larger with the value of wavenumbers increasing, even though the sufficiently fine mesh is applied to Helmholtz equations. Fortunately, the problem has been solved in the past researches and it has been demonstrated that the relative error of the numerical solution to Helmholtz equations can be controlled using the next equations [16]:

$$E_\eta^p \leq C_1 \kappa_p h + C_2 \kappa_p^3 h^2; \quad E_\eta^s \leq C_1 \kappa_s h + C_2 \kappa_s^3 h^2, \quad (5.2)$$

where C_1 and C_2 are the related constants, which are independent of the characteristic length h and the wavenumbers κ_p or κ_s . According to Eq. (2.3), we can know that κ_p and κ_s are related to λ and μ . Let the same constants $\lambda=2$ and $\mu=1$ in this paper. Meanwhile, we adopt a single compressional plane wave with the incident angle $\phi=0$ to illuminate the obstacle in this paper.

In this work, the characteristic length of triangular (T3) and quadrilateral (Q4) element are evaluated by

$$h_{T3} = \sqrt{2A_\Omega/N_e}, \quad h_{Q4} = \sqrt{A_\Omega/N_e}, \quad (5.3)$$

where N_e is the number of triangular or quadrilateral elements, A_Ω is the area of problem domain.

In addition, to apply the TBC in next numerical experiments, the infinite Fourier series in Eqs. (3.15) and (3.16) needs to be truncated, and can be re-given:

$$\begin{aligned} \mathbf{K}_{IJ}^1 &= \int_{\Gamma_B} \mathbf{N}_I \mathbf{M}_1 \mathbf{N}_J d\Gamma \\ &= - \sum_{j=0}^{N_{opt}} \frac{\kappa_p}{\pi} \frac{H_n^{(1)'(\kappa_p R)}}{H_n^{(1)}(\kappa_p R)} \left(\int_{\Gamma_B} \mathbf{N}_I(\mathbf{x}) F_j(\mathbf{x}) d\Gamma \right) \times \left(\int_{\Gamma_B} \mathbf{N}_J(\mathbf{x}) F_j(\mathbf{x}') d\Gamma \right), \end{aligned} \quad (5.4)$$

$$\begin{aligned} \mathbf{K}_{IJ}^2 &= \int_{\Gamma_B} \mathbf{N}_I \mathbf{M}_2 \mathbf{N}_J d\Gamma \\ &= - \sum_{j=0}^{N_{opt}} \frac{\kappa_s}{\pi} \frac{H_n^{(1)'(\kappa_s R)}}{H_n^{(1)}(\kappa_s R)} \left(\int_{\Gamma_B} \mathbf{N}_I(\mathbf{x}) F_j(\mathbf{x}) d\Gamma \right) \times \left(\int_{\Gamma_B} \mathbf{N}_J(\mathbf{x}) F_j(\mathbf{x}') d\Gamma \right), \end{aligned} \quad (5.5)$$

where N_{opt} is an appropriate truncated number.

Furthermore, the radius R of the boundary Γ_B is also a crucial parameter for the accuracy of the elastic wave scattering problem. If the value of R is large, it is useful to enhance the accuracy of the numerical solution. But when the value is too large, it can produce more expensive calculation costs. Therefore, choosing appropriate N_{opt} and R makes sense for the numerical example. According to the Refs. [54,55] and a lot of experimental results, unless otherwise specified, we directly use $N_{opt}=40$ and $R=7m$ in next numerical examples.

5.1 The elastic wave scattering by infinite cylinder with circular section

The elastic wave scattering by an infinite cylinder with circular section in this section is first studied in this section, as shown in Fig. 4. The parameter equations of circular section are:

$$x(t) = r \cos t, \quad y(t) = r \sin t, \quad (5.6)$$

where the boundary $\Gamma(t) = (x(t), y(t))$, $t \in [0, 2\pi]$.

Since the variables are unchanged along the z -axis and the dimension is much larger than that of other axes, this problem can be regarded as a typical two-dimensional problem even though the three-dimensional space is involved. Let the radius of the cylinder be $r = 2m$. The analytical solution to the elastic wave scattering by a circle-shaped obstacle has been given by Ref. [28]:

$$\phi(r, \theta) = \sum_{n \in \mathbb{Z}} \frac{H_n^{(1)}(\kappa_p r)}{H_n^{(1)}(\kappa_p R)} \phi^{(n)}(R) e^{in\theta}; \quad \psi(r, \theta) = \sum_{n \in \mathbb{Z}} \frac{H_n^{(1)}(\kappa_s r)}{H_n^{(1)}(\kappa_s R)} \psi^{(n)}(R) e^{in\theta}, \quad (5.7)$$

where

$$\phi^{(n)} = \frac{R^2 H_n^{(1)}(\kappa_p R) H_n^{(1)}(\kappa_s R)}{R^2 \kappa_p \kappa_s H_n^{(1)' }(\kappa_p R) H_n^{(1)' }(\kappa_s R) - n^2 H_n^{(1)}(\kappa_p R) H_n^{(1)}(\kappa_s R)} \left(\frac{\kappa_s H_n^{(1)' }(\kappa_s R)}{H_n^{(1)}(\kappa_s R)} f^{(n)} - \frac{in}{R} g^{(n)} \right), \quad (5.8)$$

$$\psi^{(n)} = \frac{R^2 H_n^{(1)}(\kappa_p R) H_n^{(1)}(\kappa_s R)}{R^2 \kappa_p \kappa_s H_n^{(1)' }(\kappa_p R) H_n^{(1)' }(\kappa_s R) - n^2 H_n^{(1)}(\kappa_p R) H_n^{(1)}(\kappa_s R)} \left(\frac{in}{R} f^{(n)} + \frac{\kappa_p H_n^{(1)' }(\kappa_p R)}{H_n^{(1)}(\kappa_p R)} g^{(n)} \right), \quad (5.9)$$

in which $H_n^{(1)}$ is the Hankel function of the first kind with order n ; $f^{(n)}$ and $g^{(n)}$ are

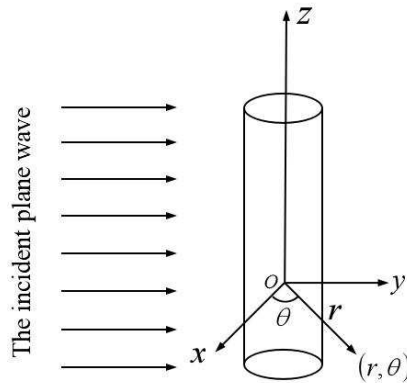


Figure 4: The plane elastic wave scattering by an infinite cylinder with circular section.

the Fourier coefficients of f and g , respectively. In particular, the detailed derivation processes are given in the appendix.

It is from Eq. (2.10) that the solution to Navier equation can be calculated by:

$$\mathbf{v} = [\mathbf{v}_1 \ \mathbf{v}_2]^T = [\partial_x \phi + \partial_y \psi \ \partial_y \phi - \partial_x \psi]^T. \quad (5.10)$$

5.1.1 Effect of angular frequency for the elastic wave scattering

In this subsection, the accuracy of the ES-FEM-T3-TBC, FEM-T3-TBC and FEM-Q4-TBC is compared at different angular frequencies for the elastic wave scattering problem. The computational domain with the TBC is discretized using the triangular elements with 1539 nodes, 2914 elements and quadrilateral elements with 1540 nodes, 1461 elements, as shown in Fig. 5.

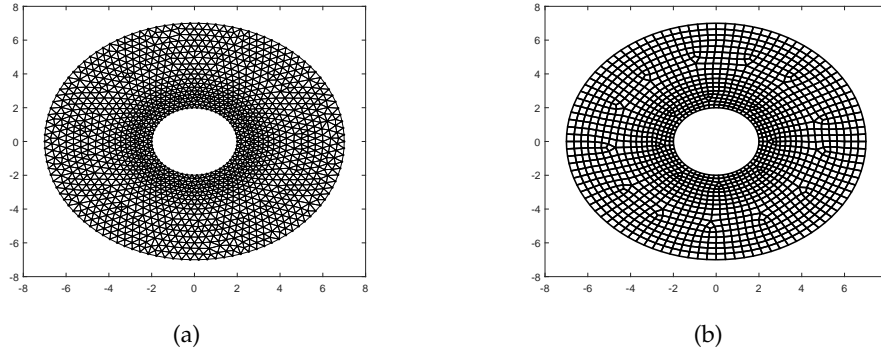


Figure 5: The used meshes for the involved computational domain: (a) triangular elements; (b) quadrilateral elements.

To take fully account of the effect of angular frequency on accuracy, several different angular frequencies are adopted, such as $\omega = 0.5, 1, 2, 3, 4, 5, 6 \text{ rad/s}$, correspondingly compressional wavenumbers $\kappa_p = 0.25, 0.5, 1, 1.5, 2, 2.5, 3 \text{ m}^{-1}$ and shear wavenumbers $\kappa_s = 0.5, 1, 2, 3, 4, 5, 6 \text{ m}^{-1}$. Based on different angular frequencies, the relative errors of (ϕ, ψ) for Helmholtz equations and (v_1, v_2) for Navier equation are listed in Tables 1, 2 and Fig. 6(a) and (b), respectively. Meanwhile, the relative errors of the total field (u_1, u_2) are also listed in Table 3 at the circle $r = 4m$.

Observing the above-mentioned results, we can easily find that the relative errors of the ES-FEM-T3-TBC are not only significantly lower than that of the FEM-T3-TBC, but also lower than that of the FEM-Q4-TBC. Meanwhile, it is also seen that the performance of three methods will all deteriorate gradually with the angular frequency increasing. However, compared to the two standard FEMs, the results of the ES-FEM-T3-TBC is more accurate and stable.

Moreover, the polar angle is compared about (ϕ, ψ) and (v_1, v_2) at $\omega = 0.5$ and 4 rad/s at the circle $r = 4m$, which are shown in Figs. 7, 8 and Figs. 9, 10.

From Figs. 7, 8 and Figs. 9, 10, some conclusions are found:

Table 1: The relative errors of (ϕ, ψ) at different angular frequencies using different methods for the elastic wave scattering by a circle-shaped obstacle.

At the circle $r=4$							
Method	$\omega=0.5$	$\omega=1$	$\omega=2$	$\omega=3$	$\omega=4$	$\omega=5$	$\omega=6$
FEM-T3-TBC	0.0392	0.0401	0.0455	0.0788	0.1570	0.3283	0.4064
FEM-Q4-TBC	0.0239	0.0214	0.0342	0.0652	0.1190	0.2852	0.3431
ES-FEM-T3-TBC	0.0205	0.0199	0.0295	0.0413	0.0739	0.1089	0.2691
At the circle $r=6$							
FEM-T3-TBC	0.0346	0.0360	0.0798	0.1845	0.3944	0.6871	0.9605
FEM-Q4-TBC	0.0258	0.0246	0.0599	0.1521	0.3414	0.6109	0.8059
ES-FEM-T3-TBC	0.0223	0.0207	0.0361	0.0509	0.1289	0.1415	0.2427
At the total computational domain							
FEM-T3-TBC	0.0578	0.1282	0.0613	0.1222	0.2313	0.3964	0.5725
FEM-Q4-TBC	0.0298	0.0256	0.0474	0.1059	0.1917	0.3466	0.4776
ES-FEM-T3-TBC	0.0233	0.0227	0.0338	0.0470	0.0938	0.1119	0.2536

Table 2: The relative errors of (v_1, v_2) at different angular frequencies using different methods for the elastic wave scattering by a circle-shaped obstacle.

At the circle $r=4$							
Method	$\omega=0.5$	$\omega=1$	$\omega=2$	$\omega=3$	$\omega=4$	$\omega=5$	$\omega=6$
FEM-T3-TBC	0.0336	0.0453	0.0803	0.1486	0.2648	0.3831	0.6021
FEM-Q4-TBC	0.0235	0.0282	0.0629	0.1243	0.2266	0.3294	0.4463
ES-FEM-T3-TBC	0.0200	0.0248	0.0428	0.0684	0.0994	0.1930	0.3131
At the circle $r=6$							
FEM-T3-TBC	0.0335	0.0486	0.1427	0.3004	0.5186	0.7914	1.0562
FEM-Q4-TBC	0.0197	0.0305	0.1231	0.2584	0.4580	0.7352	1.0080
ES-FEM-T3-TBC	0.0212	0.0291	0.0615	0.0985	0.1741	0.2924	0.3254
At the total computational domain							
FEM-T3-TBC	0.0536	0.0880	0.1222	0.2227	0.3751	0.5447	0.6676
FEM-Q4-TBC	0.0630	0.0522	0.1053	0.1947	0.3293	0.4964	0.6002
ES-FEM-T3-TBC	0.0338	0.0396	0.0707	0.1095	0.1575	0.2292	0.3052

Table 3: The relative errors of (u_1, u_2) at different angular frequencies using different methods for the elastic wave scattering by a circle-shaped obstacle.

At the circle $r=4$							
Method	$\omega=0.5$	$\omega=1$	$\omega=2$	$\omega=3$	$\omega=4$	$\omega=5$	$\omega=6$
FEM-T3-TBC	0.0278	0.0249	0.0496	0.1266	0.1791	0.2400	0.3827
FEM-Q4-TBC	0.0194	0.0155	0.0389	0.1059	0.1532	0.2064	0.2837
ES-FEM-T3-TBC	0.0165	0.0136	0.0265	0.0583	0.0672	0.1209	0.1990

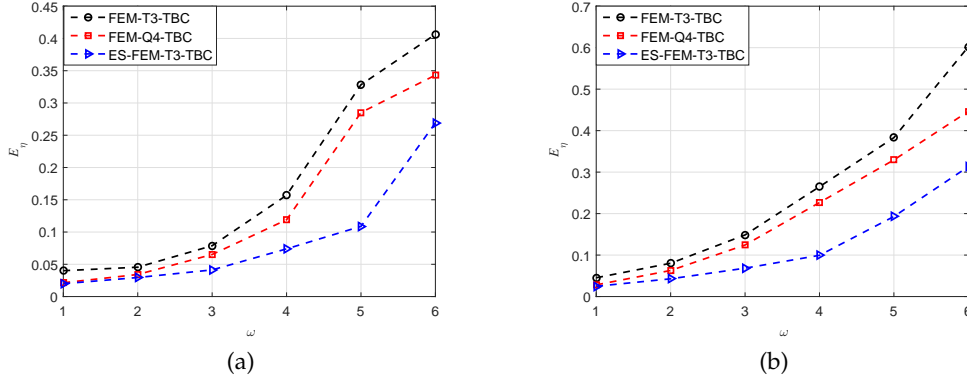


Figure 6: (a) The relative errors of (ϕ, ψ) at different angular frequencies using different methods at the circle $r = 4m$; (b) the relative errors of (v_1, v_2) at different angular frequencies using different methods at the circle $r = 4m$.

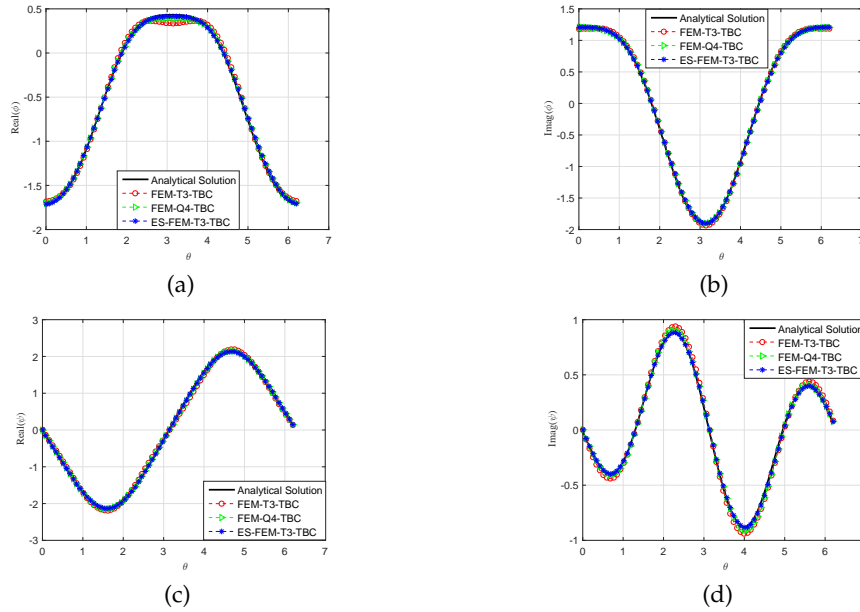


Figure 7: The results obtained using the FEM-T3-TBC, FEM-Q4-TBC and ES-FEM-T3-TBC at $\omega = 0.5 \text{ rad/s}$ for the elastic wave scattering by a circle-shaped obstacle: (a) the real part of ϕ ; (b) the imaginary part of ϕ ; (c) the real part of ψ ; (d) the imaginary part of ψ .

1. At $\omega = 0.5 \text{ rad/s}$, these numerical results from three different methods have very similar accuracy with the analytical solution.
2. The solution ϕ is better than ψ at $\omega = 4 \text{ rad/s}$, which confirms the conclusion given in Eq. (5.2) that the relative errors are controlled mainly by shear wavenumber κ_s for the elastic wave scattering.

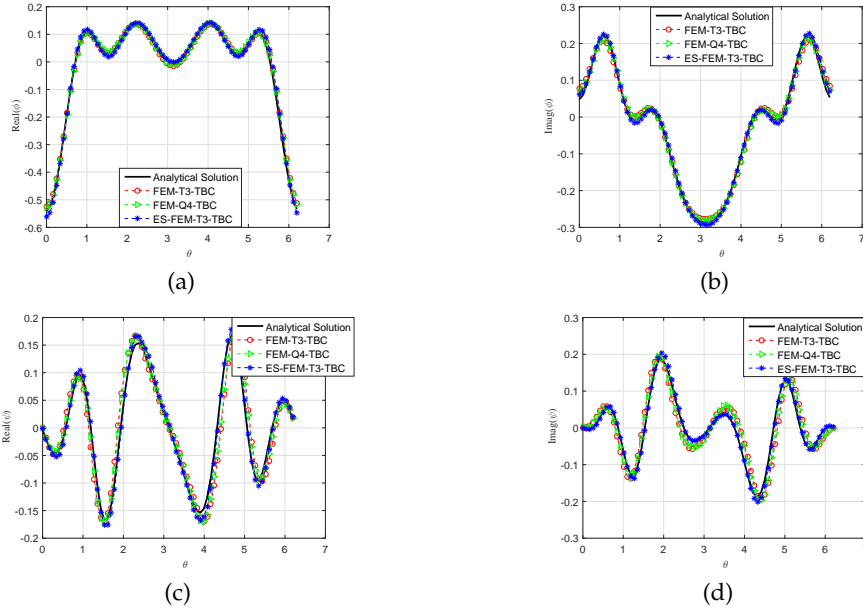


Figure 8: The results obtained using the FEM-T3-TBC, FEM-Q4-TBC and ES-FEM-T3-TBC at $\omega = 4 \text{ rad/s}$ for the elastic wave scattering by a circle-shaped obstacle: (a) the real part of ϕ ; (b) the imaginary part of ϕ ; (c) the real part of ψ ; (d) the imaginary part of ψ .

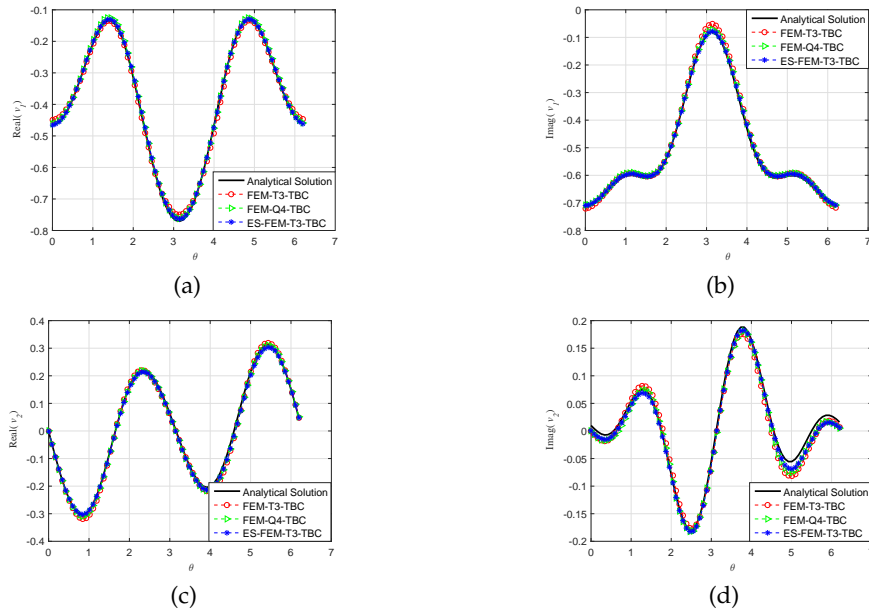


Figure 9: The results obtained using the FEM-T3-TBC, FEM-Q4-TBC and ES-FEM-T3-TBC at $\omega = 0.5 \text{ rad/s}$ for the elastic wave scattering by a circle-shaped obstacle: (a) the real part of v_1 ; (b) the imaginary part of v_1 ; (c) the real part of v_2 ; (d) the imaginary part of v_2 .

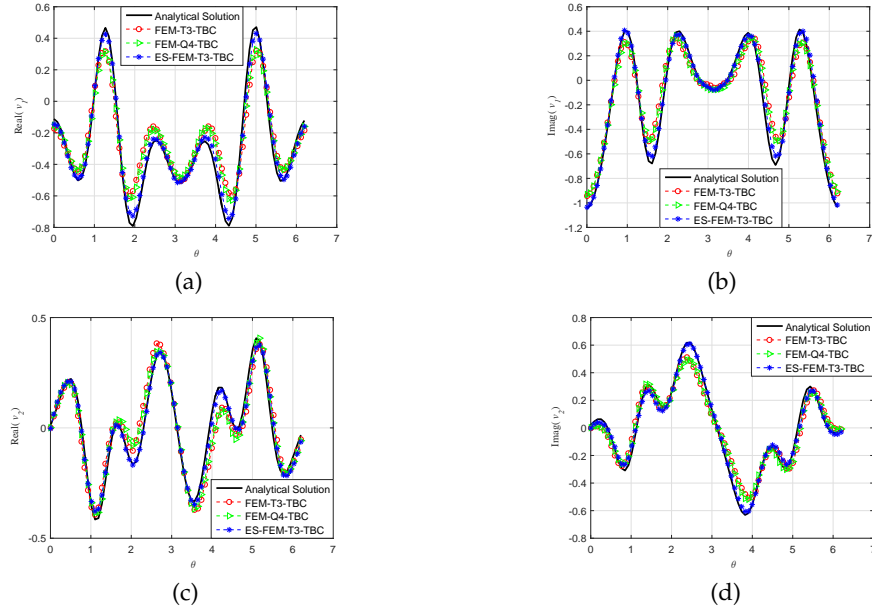


Figure 10: The results obtained using the FEM-T3-TBC, FEM-Q4-TBC and ES-FEM-T3-TBC at $\omega = 4 \text{ rad/s}$ for the elastic wave scattering by a circle-shaped obstacle: (a) the real part of v_1 ; (b) the imaginary part of v_1 ; (c) the real part of v_2 ; (d) the imaginary part of v_2 .

- From the above-mentioned results, we can find that based on the same size of meshes, with the increasing of angular frequency, the relative errors of the two standard FEMs increase faster than that of the ES-FEM-T3-TBC. Especially, when ω is greater than 4, the relative errors of the two standard FEMs have become larger. However, the relative errors of the ES-FEM-T3-TBC are still lower. Therefore, compared to the two standard FEMs, the angular frequency of the ES-FEM-T3-TBC can have a larger range, which implies the ES-FEM-T3-TBC is not sensitive relatively to the angular frequency.

5.1.2 Effect of different domain truncation methods

The effects of two different domain truncation methods (PML and TBC) on the accuracy for the elastic wave scattering are considered in this subsection. In the example, the accuracy of results of the ES-FEM-T3-TBC and ES-FEM-T3-PML are compared based on the similar number of nodes in the background mesh. The parameters of the PML are the same as in Ref. [28]. Fig. 11 shows that the discretized meshes of the bounded domain with the TBC (1370 nodes and 2573 triangular elements) and the PML (1372 nodes and 2574 triangular elements).

The angular frequencies, compressional and shear wavenumbers are set as Subsection 5.1.1. The relative errors of (ϕ, ψ) are listed in Table 4 at the circle $r = 4m$ using the FEM-T3-PML, FEM-T3-TBC, ES-FEM-T3-PML and ES-FEM-T3-TBC.

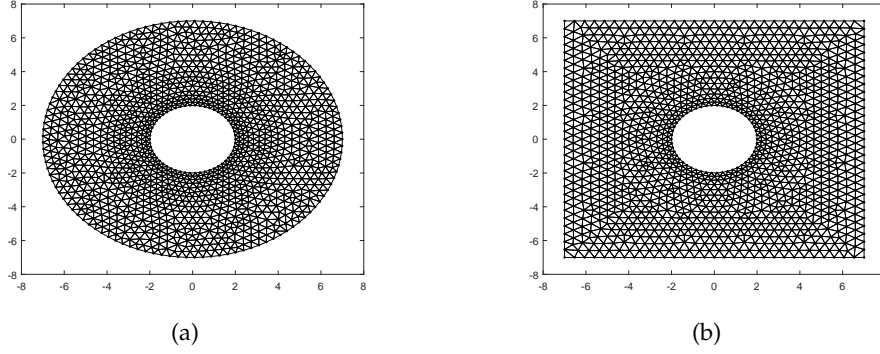


Figure 11: The discretized meshes using triangular elements in computation domain: (a) a bounded domain with the TBC; (b) a bounded domain with the PML.

Table 4: The relative errors of (ϕ, ψ) using different domain truncation methods for the elastic wave scattering by a circle-shaped obstacle.

Method	$\omega=0.5$	$\omega=1$	$\omega=2$	$\omega=3$	$\omega=4$	$\omega=5$	$\omega=6$
FEM-T3-PML	0.0598	0.0360	0.0664	0.1241	0.2413	0.3790	0.6380
FEM-T3-TBC	0.0450	0.0283	0.0509	0.1021	0.1943	0.3692	0.5162
ES-FEM-T3-PML	0.0202	0.0254	0.0367	0.0736	0.1127	0.2050	0.3451
ES-FEM-T3-TBC	0.0203	0.0198	0.0314	0.0491	0.0844	0.1134	0.3021

From Table 4, it is found that the results of ES-FEM-T3 are superior to that of the FEM-T3 for the elastic wave scattering problem regardless of truncation method. However, with the angular frequency increasing, the difference of relative error of the ES-FEM-T3 belonging to different domain truncation method will become large.

Fig. 12 and Fig. 13 show that (ϕ, ψ) compares the polar angle at $\omega=0.5$ and 4 rad/s at the circle $r=4m$, respectively.

It is seen from these figures that the relative errors of (ϕ, ψ) are very alike at $\omega=0.5 \text{ rad/s}$, but for $\omega=4 \text{ rad/s}$, we can find the results based on the TBC are better obviously than that of the PML. Therefore, if considering the accuracy of solution to the elastic wave scattering problem based on the similar number of nodes, the ES-FEM-T3-TBC is more accurate and an alternative to the ES-FEM-T3-PML, which can solve efficiently the elastic wave scattering problem [28].

5.1.3 Effect of mesh distortion for Helmholtz equations

In generally, mesh quality has a great effect on the accuracy of the numerical results. Hence, the effect of mesh distortion on the accuracy using different methods (FEM-T3-TBC and ES-FEM-T3-TBC) is compared in the subsection. Eq. (5.12) is used to obtain the irregular mesh from the regular mesh:

$$x' = x + \Delta x \cdot r_c \cdot \beta, \quad y' = y + \Delta y \cdot r_c \cdot \beta, \quad (5.11)$$

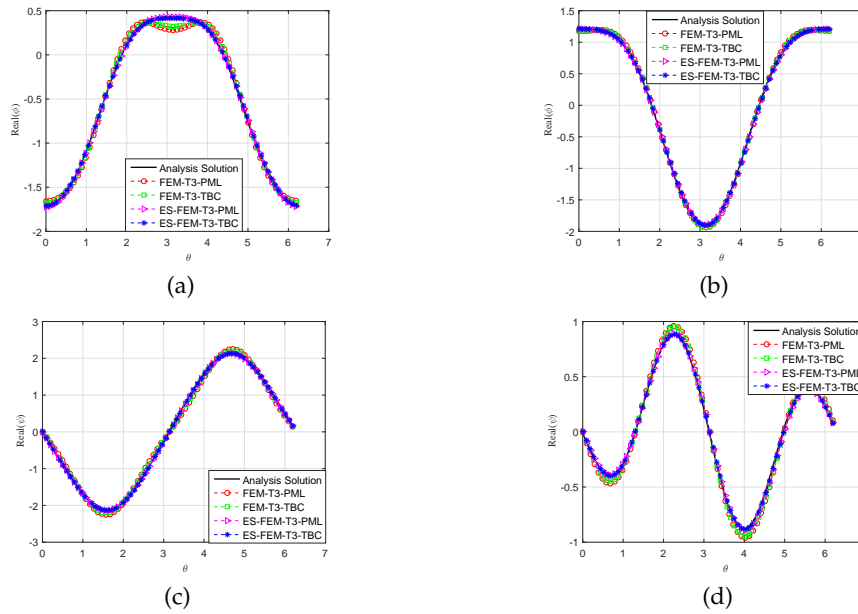


Figure 12: The results obtained using the FEM-T3-PML, FEM-T3-TBC, ES-FEM-T3-PML and ES-FEM-T3-TBC at $\omega=0.5 \text{ rad/s}$ for the elastic wave scattering by a circle-shaped obstacle: (a) the real part of ϕ ; (b) the imaginary part of ϕ ; (c) the real part of ψ ; (d) the imaginary part of ψ .

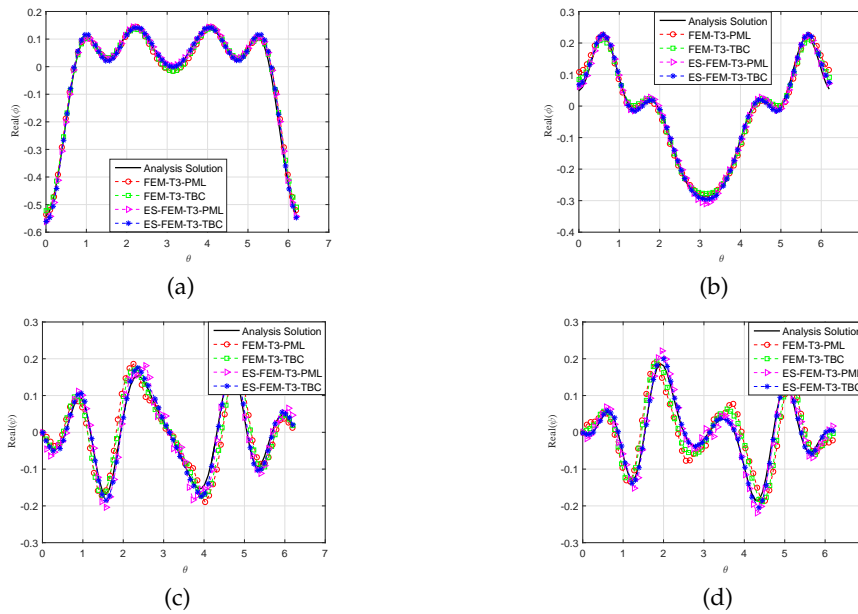


Figure 13: The results obtained using the FEM-T3-PML, FEM-T3-TBC, ES-FEM-T3-PML and ES-FEM-T3-TBC at $\omega=4 \text{ rad/s}$ for the elastic wave scattering by a circle-shaped obstacle: (a) the real part of ϕ ; (b) the imaginary part of ϕ ; (c) the real part of ψ ; (d) the imaginary part of ψ .

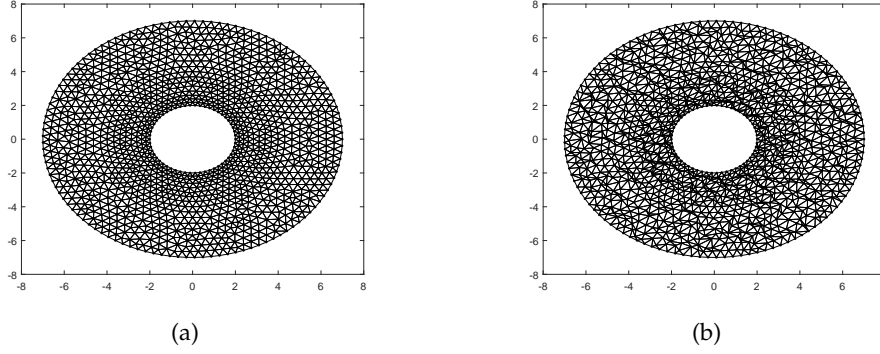


Figure 14: (a) The used regular mesh; (b) the corresponding irregular mesh at $\beta=0.5$ for the elastic wave scattering by a circle-shaped obstacle.

Table 5: The relative errors of (ϕ, ψ) using different methods at different irregular factors for the elastic wave scattering problem by a circle-shaped obstacle.

Method	$\beta=0.0$	$\beta=0.1$	$\beta=0.2$	$\beta=0.3$	$\beta=0.4$	$\beta=0.5$
FEM-T3-TBC	0.0450	0.0462	0.0505	0.0609	0.0868	0.2105
ES-FEM-T3-TBC	0.0203	0.0204	0.0205	0.0209	0.0223	0.0237

where x and y represent the coordinate values of the nodes on the original regular mesh; x' and y' are the coordinate values of the nodes on the irregular mesh corresponding to x and y ; Δx and Δy show the characteristic length in the x and y directions, respectively. r_c is a random number in the interval $[-1, 1]$. β is a parameter about the irregularity factor, which can distort the mesh. The value of β ranges from 0 to 1. Fig. 14 gives the used regular mesh and the corresponding irregular mesh for $\beta=0.5$ at the angular frequency $\omega=0.5 \text{ rad/s}$.

Given the angular frequency $\omega=0.5 \text{ rad/s}$, the different irregularity factors $\beta=0.0, 0.1, 0.2, 0.3, 0.4, 0.5$ are considered here. The relative errors of (ϕ, ψ) at the circle $r=4m$ using different methods at different irregularity factors are listed in Table 5. In order to clearly identify the numerical results of different methods, the real and imaginary part of the solutions ϕ and ψ to Helmholtz equations are presented in Fig. 15.

From the above results, we can find that both the results of the FEM-T3-TBC and ES-FEM-T3-TBC will deteriorate with the irregular factor increasing, but the speed of deterioration of the FEM-T3-TBC is clearly faster than that of the ES-FEM-T3-TBC. The ES-FEM-T3-TBC using irregular mesh still keep the same order with the ES-FEM-T3-TBC using regular mesh, but the results of the FEM-T3-TBC using irregular mesh is poorer than that of the regular mesh. Moreover, we can also find that the relative error of the FEM-T3-TBC is almost 9 times that of the ES-FEM-T3-TBC at $\beta=0.5$. These crucial findings fully demonstrate that the ES-FEM-T3-TBC is less sensitive to mesh distortion than the FEM-T3-TBC.

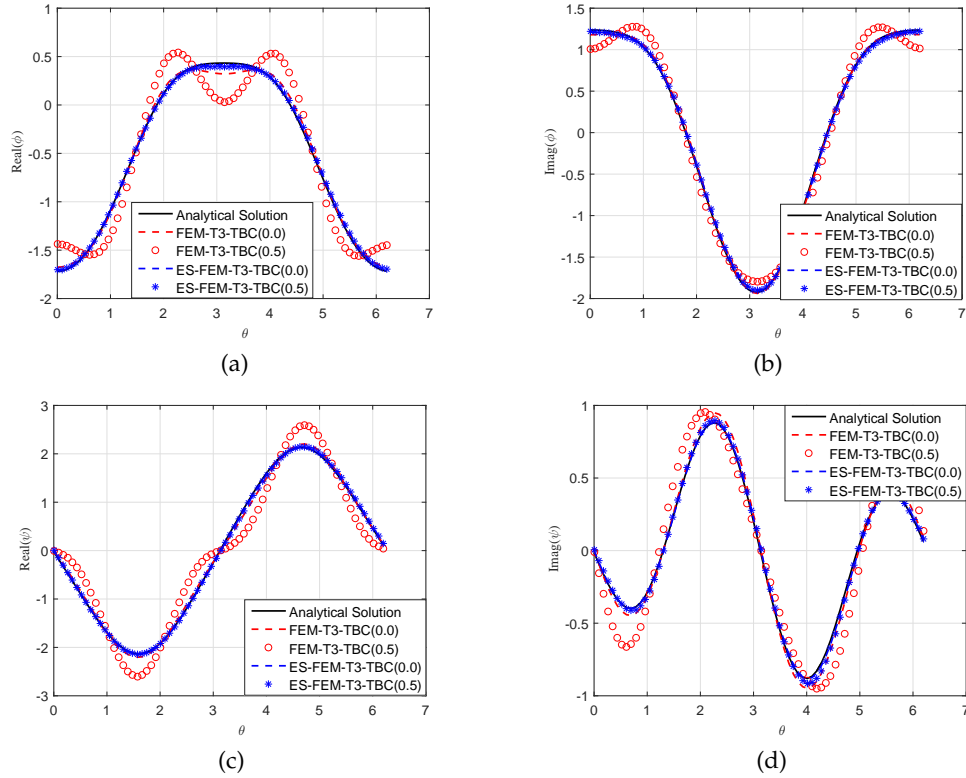


Figure 15: The (ϕ, ψ) for the elastic wave scattering problem by a circle-shaped obstacle: (a) the real part of ϕ ; (b) the imaginary part of ϕ ; (c) the real part of ψ ; (d) the imaginary part of ψ .

5.1.4 Convergence study for Helmholtz equations

In this subsection, the convergence properties of the ES-FEM-T3-TBC for the elastic wave scattering problem are studied and discussed. In order to present the convergence properties, several uniform meshes are used in the part. Given the angular frequency $\omega = 6 \text{ rad/s}$, the results of three numerical methods (FEM-T3-TBC, FEM-Q4-TBC and ES-FEM-T3-TBC) are plotted on Fig. 16. It is seen from Fig. 16(a) that as the number of nodes increases, the relative errors will almost tend to three certain values for above three numerical methods. The value of the ES-FEM-T3-TBC is the smallest value of three stable values.

Furthermore, in order to study more clearly the convergence properties of the ES-FEM-T3-TBC, the convergence rate for three numerical methods at $\omega = 6 \text{ rad/s}$ are also calculated, as showed in Fig. 16(b). It is from the figure that the convergence behavior of the ES-FEM-T3-TBC ($r = 1.828$) is better than the FEM-Q4-TBC ($r = 1.4982$) and FEM-T3-TBC ($r = 1.4236$). These findings indicate that compared to the two standard FEMs, the convergence speed of the ES-FEM-T3-TBC is faster.

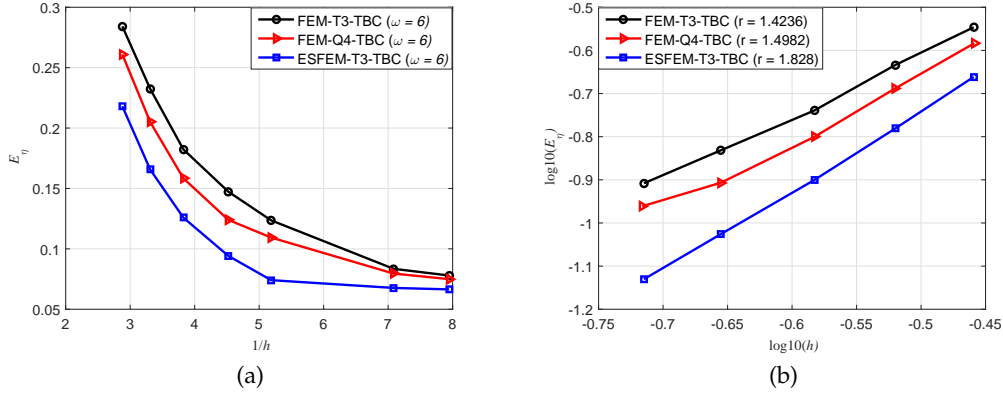


Figure 16: The convergence for solution from different methods for Helmholtz equations of the elastic wave scattering by circle shaped domain: (a) convergence of relative errors of the results; (b) convergence ratios of relative errors of the results.

5.1.5 Computational efficiency for Helmholtz equations

In this subsection, the computational efficiency of different numerical methods (FEM-T3-TBC, FEM-Q4-TBC and ES-FEM-T3-TBC) will be discussed and analyzed. In order to fully show computational efficiency, four mesh patterns are adopted for the elastic wave scattering by a circle-shaped obstacle. The details about the meshes are given in Table 6, including the number of nodes, the number of elements and the degrees of freedom for the different meshes used in the numerical experiment.

Fig. 17 shows that the computational efficiency of the FEM-T3-TBC, FEM-Q4-TBC and ES-FEM-T3-TBC at the angular frequency $\omega = 3 \text{ rad/s}$. To ensure correction of the result, we use the same direct solver to track the elastic wave scattering problem. From Fig. 17(a), it is found that the computation time of the ES-FEM-T3-TBC is higher than the two standard FEMs. But if taking the numerical error indicator into account, we can observe that the ES-FEM-T3-TBC possesses obvious advantage, as shown in Fig. 17(b). Fig. 17(b) shows that the accuracy obtained using the ES-FEM-T3-TBC with the mesh3 is the same as that using the two standard FEMs with the mesh4, but the former is

Table 6: Four meshes used in the example with a circle-shaped obstacle.

	mesh1	mesh2	mesh3	mesh4
Nodes	409(T3)	760(T3)	2897(T3)	11347(T3)
	409(Q4)	761(Q4)	2901(Q4)	11353(Q4)
Elements	714(T3)	1376(T3)	5504(T3)	22114(T3)
	360(Q4)	691(Q4)	2759(Q4)	11070(Q4)
Degrees of freedom	818(T3)	1520(T3)	5794(T3)	22694(T3)
	818(Q4)	1522(Q4)	5802(Q4)	22706(Q4)

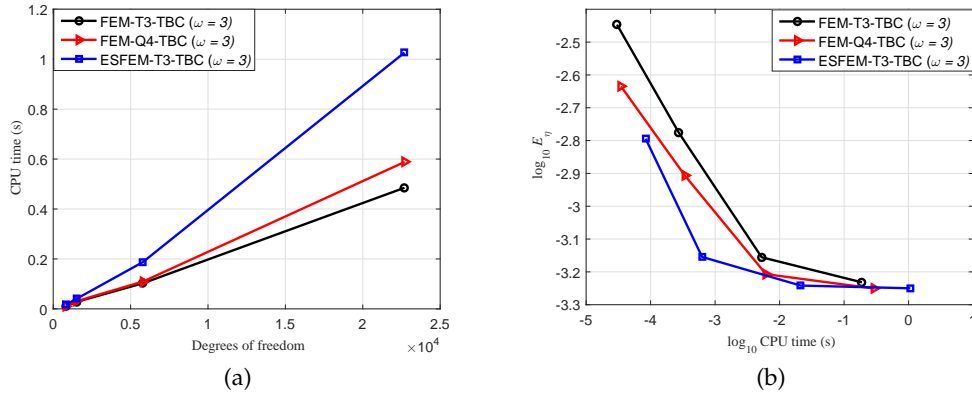


Figure 17: Comparison of computational time and efficiency among the FEM-T3-TBC, FEM-Q4-TBC and ES-FEM-T3-TBC for four meshes for the elastic wave scattering by a circle shaped obstacle: (a) the CPU time compares the degrees of freedom; (b) computational efficiency (computation time for the solution of the same accuracy).

faster for solving the problem. Therefore, the computational efficiency (CPU time for the same accuracy) of the ES-FEM-T3-TBC is higher than that of the two standard FEMs for Helmholtz equations of the elastic wave scattering problem.

5.2 The elastic wave scattering by infinite cylinder with elliptical section

The second example is concerned about the elastic wave scattering problem by an obstacle composed of an elliptical shape. The illustration about the example is shown in Fig. 18(a). The long half-axis of the ellipse section is represented by a ($a = 2m$) and b ($b = 1m$) is the short half-axis.

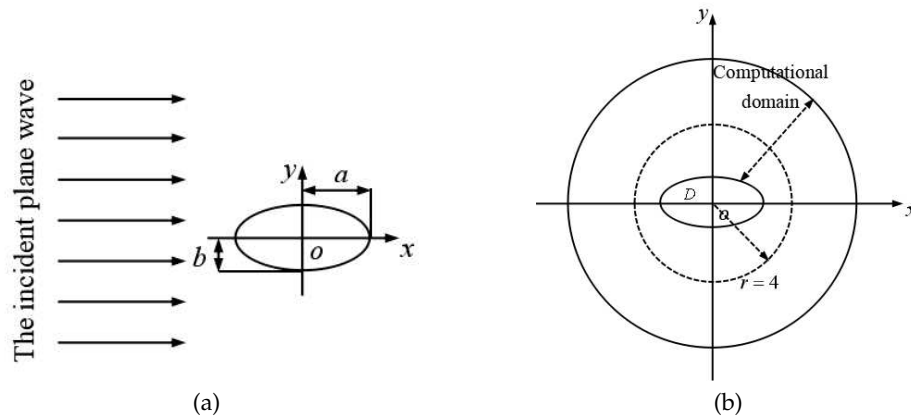


Figure 18: (a) The elastic wave scattering problem by an obstacle with ellipse shape; (b) the schematic diagram of computational domain of an obstacle with ellipse shape.

5.2.1 Effect of angular frequency for the elastic wave scattering

In the subsection, we consider the effect of angular frequency on accuracy of (ϕ, ψ) and (v_1, v_2) using the FEM-T3-TBC, FEM-Q4-TBC and ES-FEM-T3-TBC. The computational domain with TBC is discretized using triangular elements (11523 nodes and 22536 elements) and quadrilateral elements (11518 nodes and 11291 elements). Fig. 18(b) shows the schematic diagram of computational domain with TBC of an obstacle with ellipse shape. The other parameters are set as in Subsection 5.1.1. It is very difficult to find the analytical solution for this example, so the reference solution is obtained using the FEM with six-noded triangular element mesh (FEM-T6), which is a very fined mesh with 22537 nodes and 44474 elements. Several different angular frequencies $\omega = 0.5, 1, 3, 6, 9 \text{ rad/s}$ are considered here. The relative errors of (ϕ, ψ) and (v_1, v_2) at $r=4m$ are listed in Tables 7 and 8, separately.

From Tables 7 and 8, before $\omega \leq 3 \text{ rad/s}$, the relative errors of three numerical methods are all very less. But from $\omega \geq 6 \text{ rad/s}$, the results of the two standard FEMs begin to deteriorate, which are greater than 0.1. However, the relative errors of the ES-FEM-T3-TBC are always less for the elastic wave scattering problem.

Similarly, Figs. 19, 20 and Figs. 21, 22 display (ϕ, ψ) and (v_1, v_2) at $\omega = 0.5$ and 9 rad/s versus the polar angle, respectively.

These figures can show the following:

1. At $\omega = 0.5 \text{ rad/s}$, the numerical solution of three numerical methods agrees well with reference solution to the elastic wave scattering.
2. With the angular frequency increasing, (ϕ, ψ) and (v_1, v_2) of three numerical methods will deteriorate gradually. However, at $\omega = 9 \text{ rad/s}$, the results of the two standard FEMs are obviously worse than that of the ES-FEM-T3-TBC. It also shows

Table 7: The relative errors of (ϕ, ψ) at different angular frequencies at the circle $r=4m$ using different methods for the elastic wave scattering by an ellipse-shaped obstacle.

Method	$\omega = 0.5$	$\omega = 1$	$\omega = 3$	$\omega = 6$	$\omega = 9$
FEM-T3-TBC	0.0294	0.0129	0.0189	0.1143	0.3220
FEM-Q4-TBC	0.0229	0.0060	0.0166	0.1141	0.3219
ES-FEM-T3-TBC	0.0015	0.0014	0.0073	0.0317	0.1170

Table 8: The relative errors of (v_1, v_2) at different angular frequencies at the circle $r=4m$ using different methods for the elastic wave scattering by an ellipse-shaped obstacle.

Method	$\omega = 0.5$	$\omega = 1$	$\omega = 3$	$\omega = 6$	$\omega = 9$
FEM-T3-TBC	0.0219	0.0163	0.0418	0.1679	0.4567
FEM-Q4-TBC	0.0172	0.0097	0.0325	0.1539	0.4418
ES-FEM-T3-TBC	0.0050	0.0078	0.0218	0.0562	0.1430

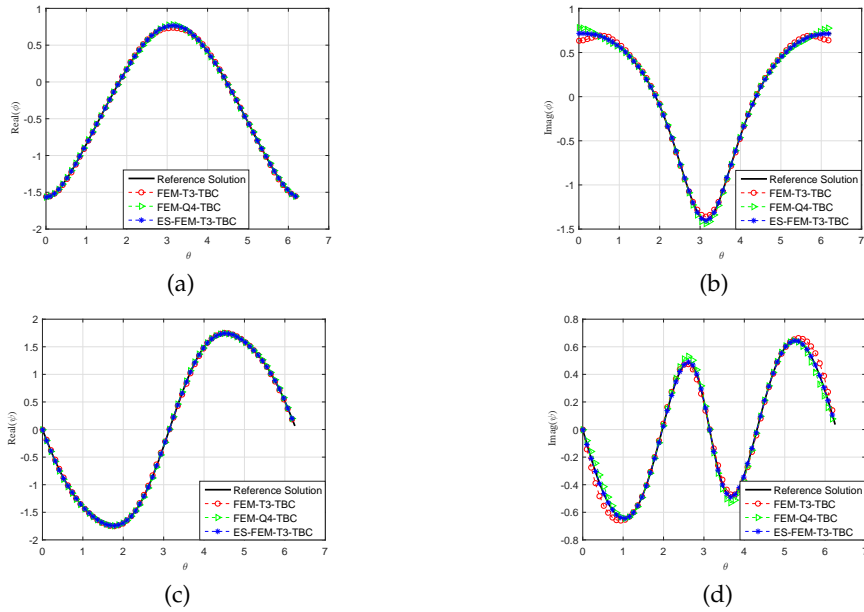


Figure 19: The results obtained using the FEM-T3-TBC, FEM-Q4-TBC and ES-FEM-T3-TBC at $\omega=0.5 \text{ rad/s}$ for the elastic wave scattering by an ellipse-shaped obstacle: (a) the real part of ϕ ; (b) the imaginary part of ϕ ; (c) the real part of ψ ; (d) the imaginary part of ψ .

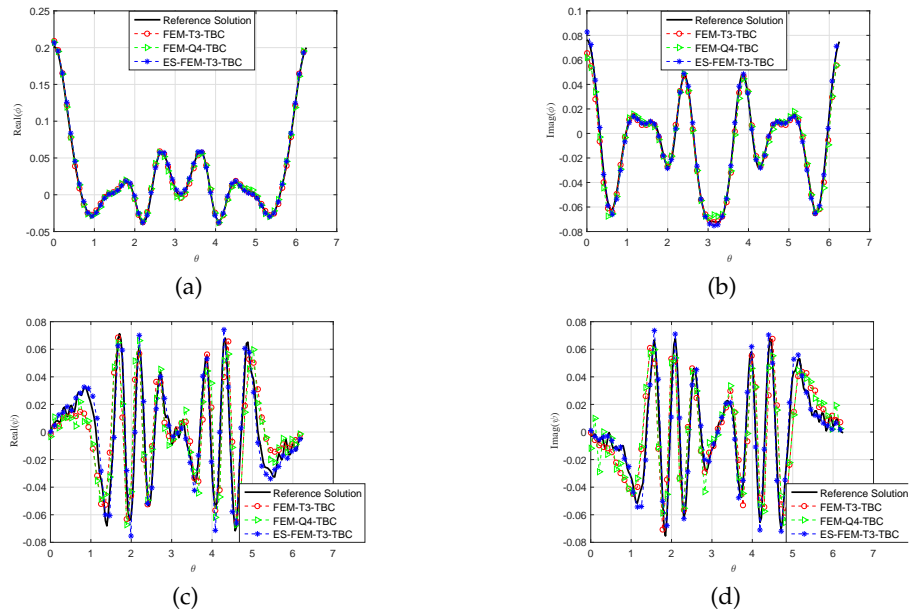


Figure 20: The results obtained using the FEM-T3-TBC, FEM-Q4-TBC and ES-FEM-T3-TBC at $\omega=9 \text{ rad/s}$ for the elastic wave scattering by an ellipse-shaped obstacle: (a) the real part of ϕ ; (b) the imaginary part of ϕ ; (c) the real part of ψ ; (d) the imaginary part of ψ .

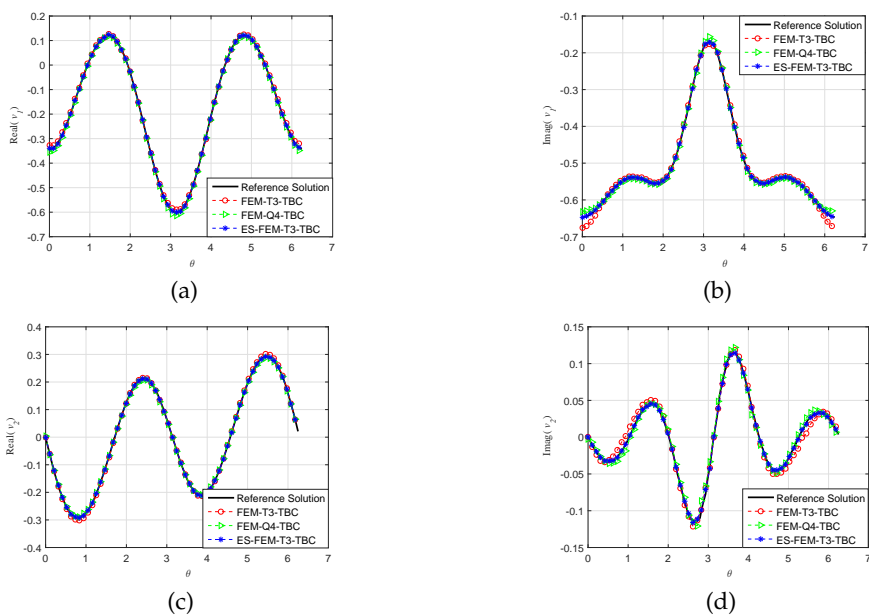


Figure 21: The results obtained using the FEM-T3-TBC, FEM-Q4-TBC and ES-FEM-T3-TBC at $\omega=0.5 \text{ rad/s}$ for the elastic wave scattering by an ellipse-shaped obstacle: (a) the real part of v_1 ; (b) the imaginary part of v_1 ; (c) the real part of v_2 ; (d) the imaginary part of v_2 .

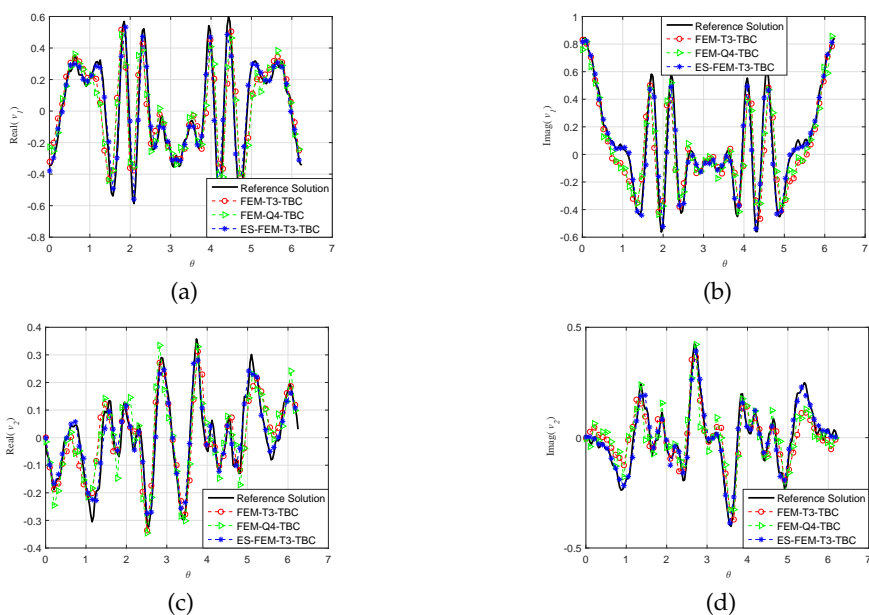


Figure 22: The results obtained using the FEM-T3-TBC, FEM-Q4-TBC and ES-FEM-T3-TBC at $\omega=9 \text{ rad/s}$ for the elastic wave scattering by an ellipse-shaped obstacle: (a) the real part of v_1 ; (b) the imaginary part of v_1 ; (c) the real part of v_2 ; (d) the imaginary part of v_2 .

again that the ES-FEM-T3-TBC is less sensitive to the angular frequency than the two standard FEMs for the elastic wave scattering.

3. From Fig. 20, it is seen that ψ is worse than ϕ , especially for the two standard FEMs. The reason is shear wavenumbers κ_s is always greater than compressional wavenumbers κ_p at the same angular frequency.

5.2.2 Effect of different domain truncation methods

This paper compares the effect of imposed different domain truncation methods (PML and TBC) on the accuracy of (ϕ, ψ) for Helmholtz equations in the subsection. The conditions of the PML is the same as in Subsection 5.1.2. The reference solution can be obtained by the FEM-T6 with the very fine mesh model (22537 nodes, 44474 elements). The computational domain with the TBC is discretized into triangular elements (11523 nodes and 22536 elements) and the computational domain with the PML is discretized into triangular elements (11523 nodes and 22546 elements). The angular frequencies are set $\omega = 0.5, 1, 3, 6, 9 \text{ rad/s}$. The relative errors of (ϕ, ψ) at the circle $r = 4m$ using the FEM-T3-PML, FEM-T3-TBC, ES-FEM-T3-PML and ES-FEM-T3-TBC are listed in Table 9.

Table 9: The relative errors of (ϕ, ψ) using different domain truncation methods for the elastic wave scattering by an ellipse-shaped obstacle.

Method	$\omega = 0.5$	$\omega = 1$	$\omega = 3$	$\omega = 6$	$\omega = 9$
FEM-T3-PML	0.2501	0.0327	0.0380	0.2184	0.6111
FEM-T3-TBC	0.0314	0.0141	0.0220	0.1366	0.4066
ES-FEM-T3-PML	0.0319	0.0030	0.0102	0.0388	0.0944
ES-FEM-T3-TBC	0.0054	0.0020	0.0080	0.0248	0.0708

According to Table 9, it is seen that with the angular frequency increasing, the performance of the FEM-T3-PML, FEM-T3-TBC, ES-FEM-T3-PML and ES-FEM-T3-TBC will deteriorate gradually. But compared to other three numerical methods, the ES-FEM-T3-TBC is more accurate and stable.

Fig. 23 and Fig. 24 show (ϕ, ψ) compares the polar angle at $\omega = 0.5$ and 9 rad/s at the circle $r = 4m$, respectively. From these figures, it can find the same conclusions as Subsection 5.1.2. Meanwhile, it is seen that the ES-FEM-T3-TBC is an effective alternative to the ES-FEM-T3-PML.

5.2.3 Convergence study for Helmholtz equations

In this part, the convergence properties of the EEM-T3-TBC, EEM-Q4-TBC and ES-FEM-T3-TBC will be considered for the elastic wave scattering problem. To show the advantages of the ES-FEM-T3-TBC, several different mesh models are used to discretize the problem domain. The reference solution can be obtained by the FEM-T6 with very fined mesh pattern (22537 nodes, 44474 elements). Given angular frequency $\omega = 3 \text{ rad/s}$, the corresponding convergence results are shown in Fig. 25 for Helmholtz equations. It is

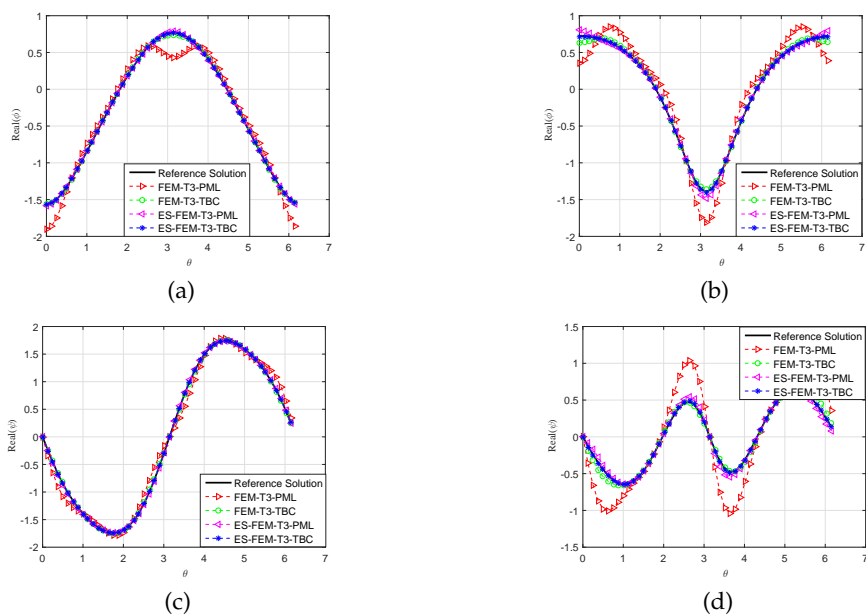


Figure 23: The results obtained using the FEM-T3-PML, FEM-T3-TBC, ES-FEM-T3-PML and ES-FEM-T3-TBC at $\omega = 0.5 \text{ rad/s}$ for the elastic wave scattering by an ellipse-shaped obstacle: (a) the real part of ϕ ; (b) the imaginary part of ϕ ; (c) the real part of ψ ; (d) the imaginary part of ψ .

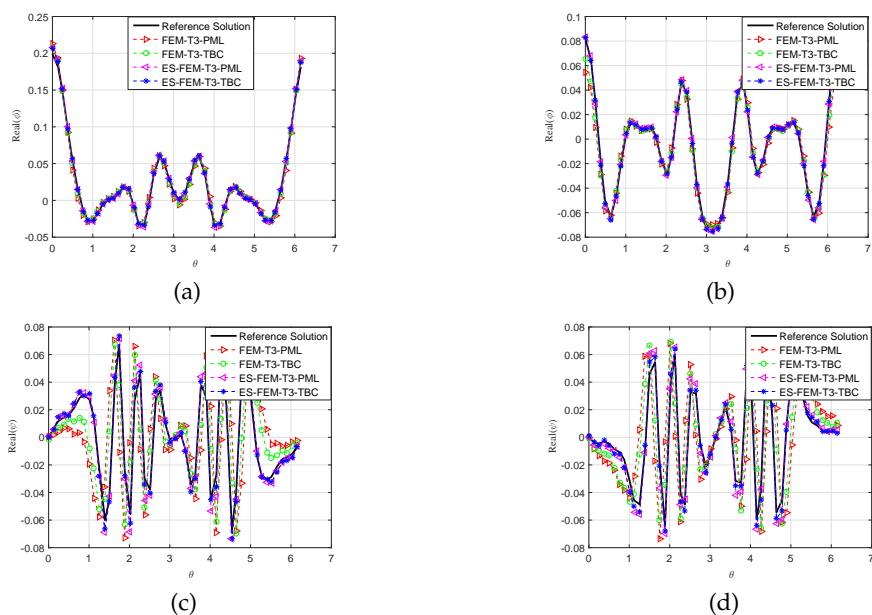


Figure 24: The results obtained using the FEM-T3-PML, FEM-T3-TBC, ES-FEM-T3-PML and ES-FEM-T3-TBC at $\omega = 9 \text{ rad/s}$ for the elastic wave scattering by an ellipse-shaped obstacle: (a) the real part of ϕ ; (b) the imaginary part of ϕ ; (c) the real part of ψ ; (d) the imaginary part of ψ .

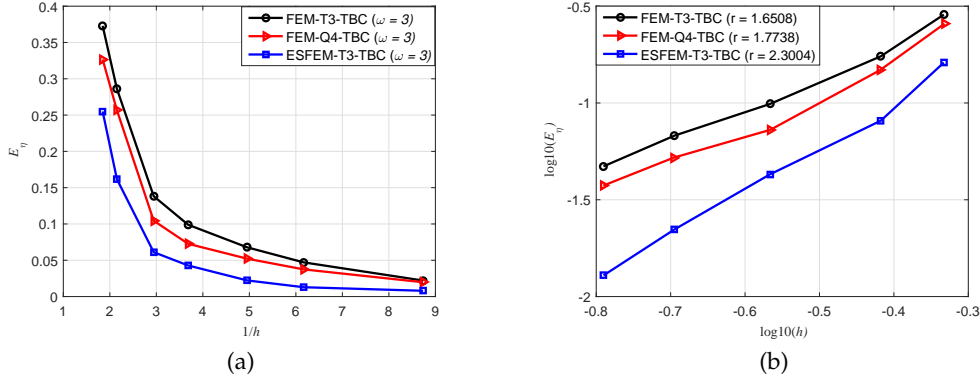


Figure 25: The convergence for solution from different methods for Helmholtz equations of the elastic wave scattering by an ellipse shaped domain: (a) convergence of relative errors of the results; (b) convergence ratios of relative errors of the results.

from Fig. 25(a) seen that three curves of relative errors among three numerical methods tend to be almost flat with the number of nodes increasing. Furthermore, the relative errors obtained by three methods converge linearly with the characteristic length of the mesh. The convergence rate of three numerical methods at $\omega = 3 \text{ rad/s}$ is calculated and as showed in Fig. 25(b). Fig. 25(b) suggests that the convergence rate of the ES-FEM-T3-TBC ($r=2.3004$) is larger than the FEM-Q4-TBC ($r=1.7738$) and FEM-T3-TBC ($r=1.6508$), which indicates that the ES-FEM-T3-TBC method has higher convergence rate and accuracy for the elastic wave scattering problem.

5.3 The elastic wave scattering by infinite cylinder with peanut section

The scattering of the plane elastic wave by an infinite cylinder with peanut section is considered as the third numerical example in this section. Fig. 26(a) shows the schematic diagram about the example. The parametric equations of peanut-shaped are:

$$x(t) = 2.3\cos(t) + 0.5\cos(3t), \quad y(t) = 2.3\sin(t) + 0.5\sin(3t), \quad (5.12)$$

where t is a parameter and $t \in [0, 2\pi]$.

5.3.1 Effect of angular frequency for the elastic wave scattering

The influence of angular frequency on the accuracy of (ϕ, ψ) and (v_1, v_2) using the FEM-T3-TBC, FEM-Q4-TBC and ES-FEM-T3-TBC is studied in the subsection. The computational domain with TBC of an obstacle with peanut shape is presented in Fig. 26(b), which is discretized using linear triangular elements (3959 nodes and 7618 elements) and quadrilateral elements (3956 nodes and 3820 elements), respectively. Likewise, the other parameters are set as in example in Subsection 5.1.1 and the reference solution can be obtained by the FEM-Q4 with very fined mesh pattern (16325 nodes and 16045 elements).

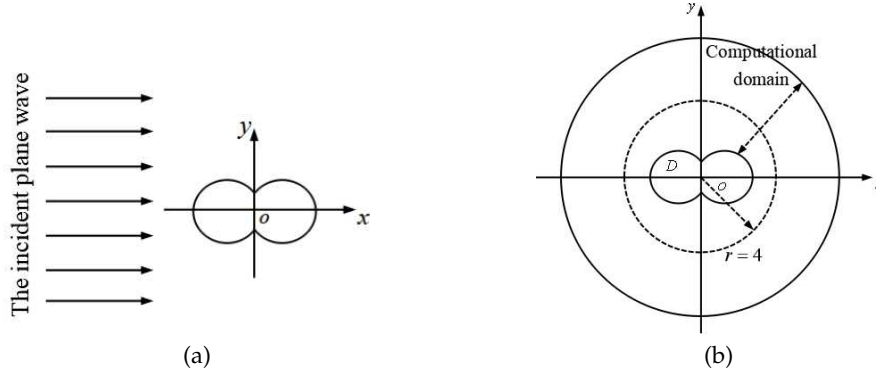


Figure 26: (a) The elastic wave scattering problem by an obstacle with peanut shape; (b) the schematic diagram of computational domain of an obstacle with peanut shape.

Table 10: The relative errors of (ϕ, ψ) at different angular frequencies using different methods for the elastic wave scattering by a peanut-shaped obstacle.

Method	$\omega=0.5$	$\omega=1$	$\omega=3$	$\omega=6$	$\omega=9$
FEM-T3-TBC	0.1732	0.0401	0.0459	0.1664	0.4616
FEM-Q4-TBC	0.0743	0.0098	0.0271	0.1266	0.4407
ES-FEM-T3-TBC	0.0173	0.0050	0.0122	0.0476	0.1605

Table 11: The relative errors of (v_1, v_2) at different angular frequencies using different methods for the elastic wave scattering by a peanut-shaped obstacle.

Method	$\omega=0.5$	$\omega=1$	$\omega=3$	$\omega=6$	$\omega=9$
FEM-T3-TBC	0.0855	0.0380	0.0797	0.2441	0.5798
FEM-Q4-TBC	0.0326	0.0133	0.0501	0.1563	0.4458
ES-FEM-T3-TBC	0.0097	0.0099	0.0264	0.0728	0.2068

Given the angular frequency $\omega = 0.5, 1, 3, 6, 9 \text{ rad/s}$, the relative errors of (ϕ, ψ) and (v_1, v_2) at the circle $r = 4m$ using different methods for the elastic wave scattering by a peanut-shaped obstacle are listed in Tables 10 and 11.

From Tables 10 and 11, we can find that the ES-FEM-T3-TBC can perform more good than the two standard FEMs, regardless of the FEM-T3-TBC or FEM-Q4-TBC. In particular, when the angular frequency is larger for the elastic wave scattering problem, the ES-FEM-T3-TBC is a satisfactory choice.

5.3.2 Convergence study for Helmholtz equations

The convergence properties of the EEM-T3-TBC, EEM-Q4-TBC and ES-FEM-T3-TBC will be studied in the subsection. To calculate the convergence property, several different mesh models are adopted to discretize the problem domain. The reference solution can be

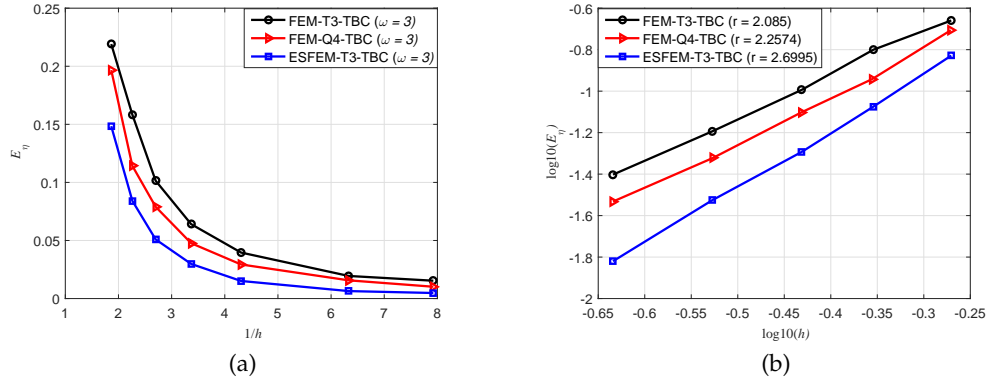


Figure 27: The convergence for solution from different methods for Helmholtz equations of the elastic wave scattering by a peanut shaped domain: (a) convergence of relative errors of the results; (b) convergence ratios of relative errors of the results.

obtained by the FEM-Q4 (16325 nodes and 16045 elements). Given the angular frequency $\omega = 3 \text{ rad/s}$, the corresponding convergence results are shown in Fig. 27. From Fig. 27(a), it can be found that the curves of three numerical methods tend almost to be three certain values with the number of nodes increasing. Fig. 27(b) shows that the convergence rate of the ES-FEM-T3-TBC ($r = 2.6995$) is more than that of the FEM-Q4-TBC ($r = 2.2574$) and FEM-T3-TBC ($r = 2.085$).

5.4 The elastic wave scattering by an obstacle with arbitrary shape

In the section, the elastic scattering problem by an obstacle with arbitrary shape is discussed, whose schematic diagram is shown in Fig. 28(a).

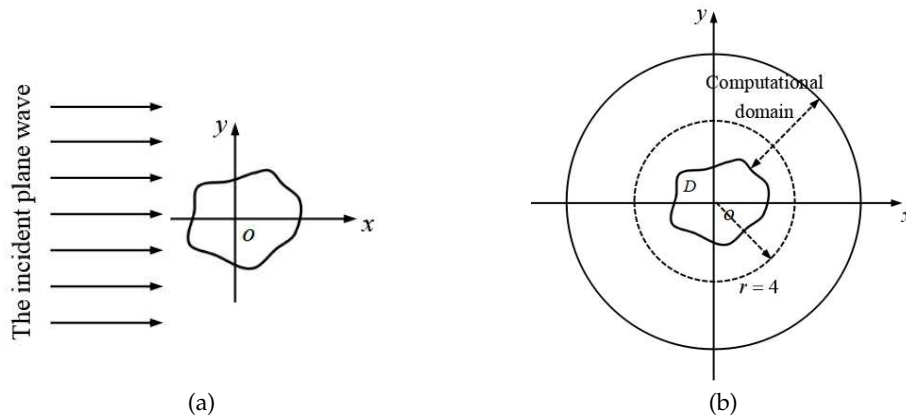


Figure 28: (a) The elastic wave scattering problem by an obstacle with arbitrary shape; (b) the schematic diagram of computational domain of an obstacle with arbitrary shape.

5.4.1 Effect of angular frequency for the elastic wave scattering

In the subsection, we still study that the effect of angular frequency on the accuracy of (ϕ, ψ) and (v_1, v_2) by the FEM-T3-TBC, FEM-Q4-TBC and ES-FEM-T3-TBC for the elastic wave scattering by an arbitrary shaped obstacle. The computational domain with TBC is discretized using linear triangular elements (3971 nodes and 7658 elements) and quadrilateral elements (3974 nodes and 3849 elements), whose schematic diagram is shown in Fig. 28(b). The other parameters are the same as the example in Subsection 5.1.1 and the reference solution can be obtained by the FEM-Q4 with 16345 nodes and 16095 elements.

Considering that the angular frequency $\omega = 0.5, 1, 3, 6, 9 \text{ rad/s}$, the relative errors of (ϕ, ψ) and (v_1, v_2) at the circle $r = 4m$ using different numerical methods are listed in Tables 12 and 13. In addition, the results (ϕ, ψ) and (v_1, v_2) are compared at $\omega = 1$ and 6 rad/s , which are displayed in Figs. 29, 30 and Figs. 31, 32.

Table 12: The relative errors of (ϕ, ψ) at different angular frequencies using different methods for the elastic wave scattering by an arbitrary-shaped obstacle.

Method	$\omega = 0.5$	$\omega = 1$	$\omega = 3$	$\omega = 6$	$\omega = 9$
FEM-T3-TBC	0.1292	0.0695	0.2920	0.2107	0.5013
FEM-Q4-TBC	0.0497	0.0942	0.0410	0.1775	0.4017
ES-FEM-T3-TBC	0.0491	0.0419	0.0372	0.0574	0.2014

Table 13: The relative errors of (v_1, v_2) at different angular frequencies using different methods for the elastic wave scattering by an arbitrary-shaped obstacle.

Method	$\omega = 0.5$	$\omega = 1$	$\omega = 3$	$\omega = 6$	$\omega = 9$
FEM-T3-TBC	0.0935	0.0727	0.4281	0.2930	0.7154
FEM-Q4-TBC	0.0468	0.0983	0.0706	0.2400	0.5999
ES-FEM-T3-TBC	0.0431	0.0460	0.0605	0.0841	0.2892

From these results, we can find that though the accuracy for the elastic wave scattering decreases when the obstacle is a asymmetric and arbitrary shape, the ES-FEM-T3-TBC can still obtain a higher accuracy than that of the two standard FEMs. Moreover, the similar conclusions with other three numerical examples can be also obtained. In other words, at small angular frequency, i.e. $\omega = 1 \text{ rad/s}$, the numerical solution is nearly agreement with reference solution for three numerical methods. However, as the angular frequency increases, especially, at $\omega = 6 \text{ rad/s}$, the results of the ES-FEM-T3-TBC are obviously superior to that of the two standard FEMs.

5.4.2 Computational efficiency for Helmholtz equations

In this subsection, the computational efficiency of the FEM-T3-TBC, FEM-Q4-TBC and ES-FEM-T3-TBC is considered. Similarly, in order to illustrate computational efficiency,

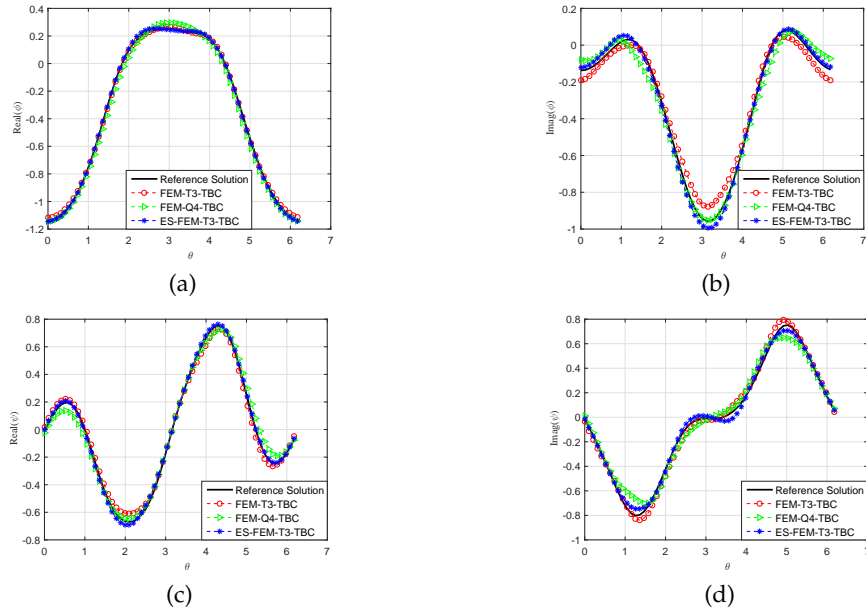


Figure 29: The results obtained using the FEM-T3-TBC, FEM-Q4-TBC and ES-FEM-T3-TBC at $\omega = 1 \text{ rad/s}$ for the elastic wave scattering by an arbitrary-shaped obstacle: (a) the real part of ϕ ; (b) the imaginary part of ϕ ; (c) the real part of ψ ; (d) the imaginary part of ψ .

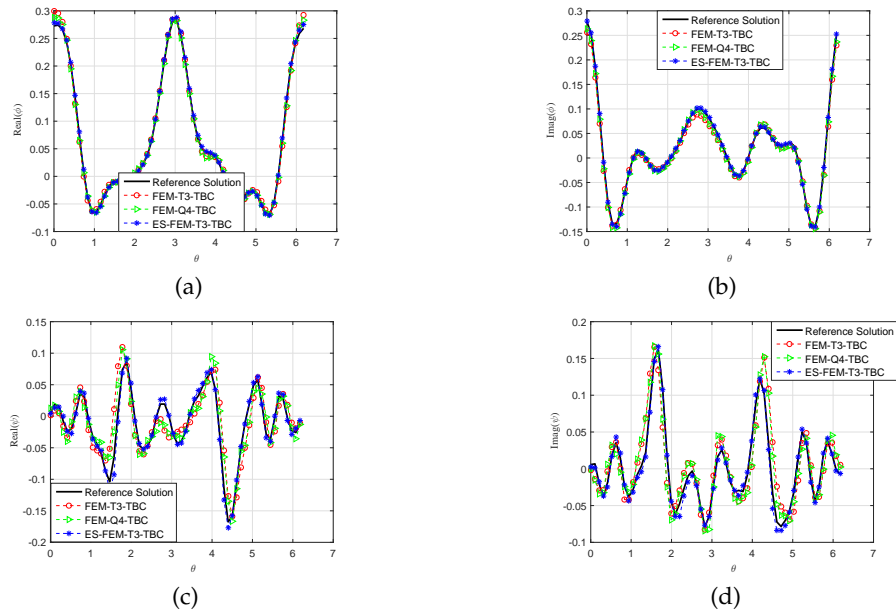


Figure 30: The results obtained using the FEM-T3-TBC, FEM-Q4-TBC and ES-FEM-T3-TBC at $\omega = 6 \text{ rad/s}$ for the elastic wave scattering by an arbitrary-shaped obstacle: (a) the real part of ϕ ; (b) the imaginary part of ϕ ; (c) the real part of ψ ; (d) the imaginary part of ψ .

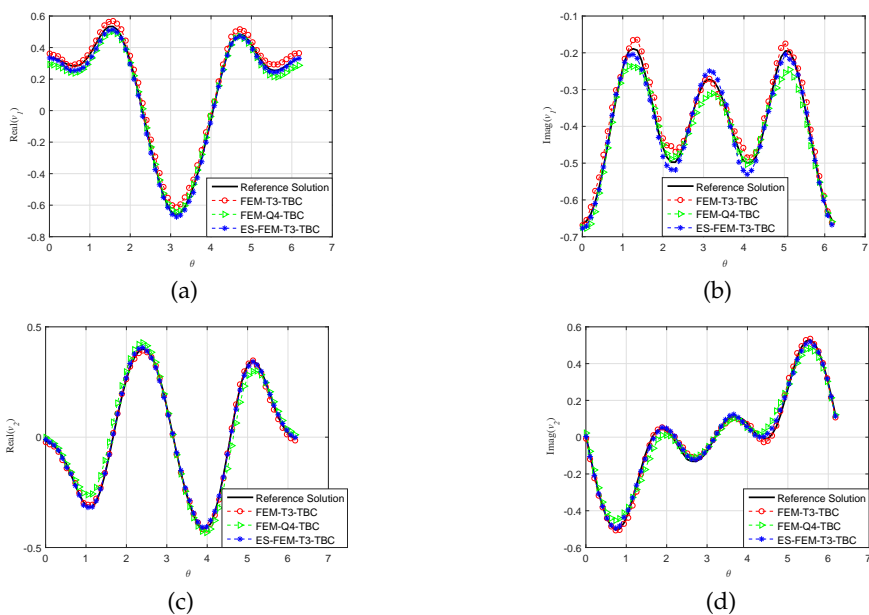


Figure 31: The results obtained using the FEM-T3-TBC, FEM-Q4-TBC and ES-FEM-T3-TBC at $\omega = 1 \text{ rad/s}$ for the elastic wave scattering by an arbitrary-shaped obstacle: (a) the real part of v_1 ; (b) the imaginary part of v_1 ; (c) the real part of v_2 ; (d) the imaginary part of v_2 .

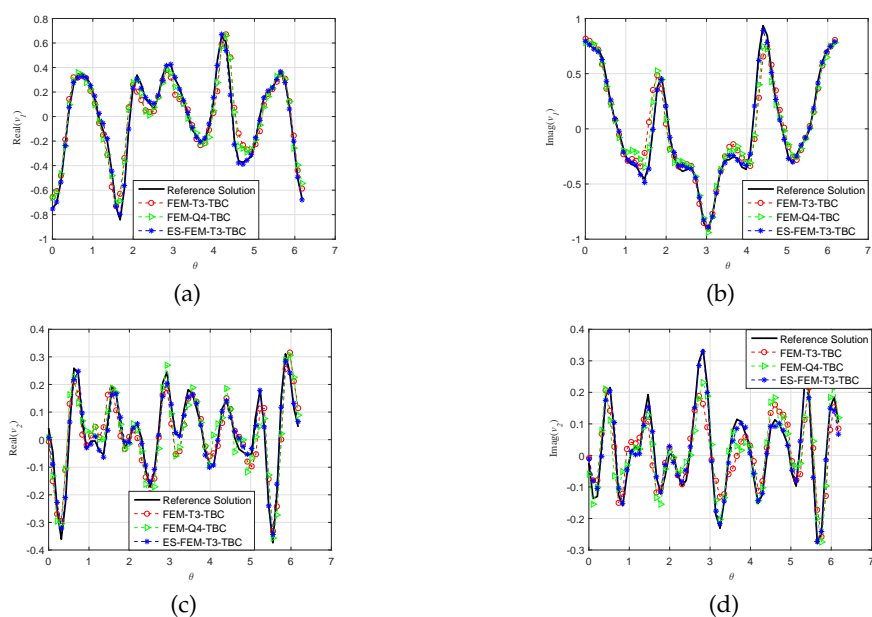


Figure 32: The results obtained using the FEM-T3-TBC, FEM-Q4-TBC and ES-FEM-T3-TBC at $\omega = 6 \text{ rad/s}$ for the elastic wave scattering by an arbitrary-shaped obstacle: (a) the real part of v_1 ; (b) the imaginary part of v_1 ; (c) the real part of v_2 ; (d) the imaginary part of v_2 .

Table 14: Four meshes used in the example with an arbitrary-shaped obstacle.

	mesh1	mesh2	mesh3	mesh4
Nodes	544(T3)	764(T3)	2811(T3)	10176(T3)
	543(Q4)	767(Q4)	2815(Q4)	10182(Q4)
Elements	980(T3)	1397(T3)	5365(T3)	19844(T3)
	492(Q4)	706(Q4)	2696(Q4)	9962(Q4)
Degrees of freedom	1088(T3)	1528(T3)	5622(T3)	20352(T3)
	1086(Q4)	1534(Q4)	5630(Q4)	20364(Q4)

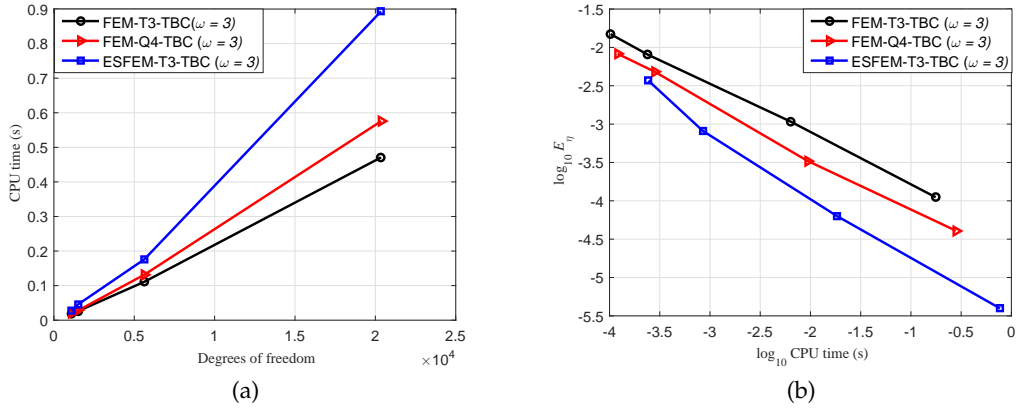


Figure 33: Comparison of computational time and efficiency among the FEM-T3-TBC, FEM-Q4-TBC and ESFEM-T3-TBC methods for four meshes for the elastic wave scattering by an arbitrary shaped obstacle: (a) the CPU time compares the degrees of freedom; (b) computational efficiency (computation time for the solution of the same accuracy).

four mesh patterns are applied here. The details about the meshes are given in Table 14, including the number of nodes, the number of elements and the degrees of freedom for the different meshes used in the numerical experiment.

The results of computational efficiency using FEM-T3-TBC, FEM-Q4-TBC and ESFEM-T3-TBC based on the same direct solver at the angular frequency $\omega = 3 \text{ rad/s}$ are shown in Fig. 33. Fig. 33(a) shows the CPU time versus the degrees of freedom and Fig. 33(b) shows the variety of the numerical error indicators with the CPU time for the three numerical methods. From these results, while the CPU time of the ES-FEM-T3-TBC is longer than that of the two standard FEMs, the computational efficiency of the ES-FEM-T3-TBC is higher than that of the two standard FEMs at the similar number of mesh nodes. That is to say, for the elastic wave scattering problem, the computational cost of the ES-FEM-T3-TBC is much less than the two standard FEMs for the same accuracy of numerical solution.

6 Conclusions

In this work, an ES-FEM-T3-TBC is presented to solve Helmholtz equations with coupled boundary conditions for the elastic wave scattering by a rigid obstacle with smooth surface. Four numerical cases are shown to demonstrate the competitiveness and effectiveness of the proposed ES-FEM-T3-TBC for the elastic wave scattering problem. From these numerical results, the following conclusions can be obtained:

1. Based on the similar number of mesh nodes, compared to the FEM-T3-TBC and FEM-Q4-TBC, the ES-FEM-T3-TBC is more stable and accurate for the elastic wave scattering problem.
2. For the convergence property and computational efficiency, the ES-FEM-T3-TBC performs better than that of the two standard FEMs. Specifically, the convergence rate of the ES-FEM-T3-TBC is as high as 2.30 in Subsection 5.2.3 and 2.69 in Subsection 5.3.2.
3. Compared with the two standard FEMs using the triangular elements and quadrilateral elements, the ES-FEM-TBC is relatively insensitive to the mesh distortion and angular frequency.
4. The present ES-FEM-T3-TBC can get higher accuracy of Helmholtz equations than that of the ES-FEM-T3-PML based on the similar number of nodes and it provides a feasible alternative to the ES-FEM-T3-PML to handle the elastic wave scattering problem.
5. At the same angular frequency, the result of ψ is worse than that of ϕ for the elastic wave scattering problem.

Therefore, these findings indicate that the ES-FEM-T3-TBC is a reliable and effective method for the elastic wave scattering problem. Future work is to extend our researches to the obstacle scattering problem composed of multiple obstacles and study the influence of other boundary condition for the elastic wave scattering problem.

Acknowledgments

The project is supported by the National Youth Science Foundation of China (Grant No. 11901423), the National Natural Science Foundation of China (Grant No. 11771321), the Youth Science and Technology Research Foundation of Shanxi Province (Grant Nos. 201901D211104, 201901D211107) and the Science and Technology Innovation Programs of Higher Education institutions in Shanxi (Grant No. 2019L0317).

Appendix: Analytical solution

In the section, the analytical solution to the elastic wave scattering by a circle-shaped obstacle in Ref. [28] is given, as follows:

Firstly, to obtain easily the analytical solution, the Helmholtz equations with coupled boundary conditions Eqs. (2.12) and (2.14) can be re-given in the polar coordinates:

$$\begin{cases} \Delta\phi + \kappa_p^2\phi = 0, \quad \Delta\psi + \kappa_s^2\psi = 0, & \text{in } \Omega, \\ \partial_r\phi + \partial_\theta\psi/R = f(\theta), \quad \partial_r\psi + \partial_\theta\phi/R = g(\theta), & \text{on } \Gamma_D, \end{cases} \quad (\text{A.1})$$

where $f(\theta) = -\mathbf{v} \cdot \mathbf{u}^{inc}$; $g(\theta) = \boldsymbol{\tau} \cdot \mathbf{u}^{inc}$.

Then according to the Fourier series expansions in the polar coordinates, the analytical solution in Eq. (A.2) is obtained:

$$\phi(r, \theta) = \sum_{n \in \mathbb{Z}} \frac{H_n^{(1)}(\kappa_p r)}{H_n^{(1)}(\kappa_p R)} \phi^{(n)}(R) e^{in\theta}; \quad \psi(r, \theta) = \sum_{n \in \mathbb{Z}} \frac{H_n^{(1)}(\kappa_s r)}{H_n^{(1)}(\kappa_s R)} \psi^{(n)}(R) e^{in\theta}, \quad (\text{A.2})$$

where $H_n^{(1)}$ is the Hankel function of the first kind with order n . $\phi^{(n)}$ and $\psi^{(n)}$ are the Fourier modes of ϕ and ψ , respectively.

The solutions $\phi^{(n)}$ and $\psi^{(n)}$ in Eqs. (5.8) and (5.9) can be obtained by the following system equations:

$$\begin{cases} \frac{\kappa_p H_n^{(1)' }(\kappa_p R)}{H_n^{(1)}(\kappa_p R)} \phi^{(n)} + \frac{in}{R} \psi^{(n)} = f^{(n)}, \\ \frac{\kappa_s H_n^{(1)' }(\kappa_s R)}{H_n^{(1)}(\kappa_s R)} \psi^{(n)} - \frac{in}{R} \phi^{(n)} = g^{(n)}, \end{cases} \quad (\text{A.3})$$

where

$$f^{(n)} = \frac{1}{2\pi} \int_0^{2\pi} f(\theta) e^{-in\theta} d\theta, \quad g^{(n)} = \frac{1}{2\pi} \int_0^{2\pi} g(\theta) e^{-in\theta} d\theta, \quad (\text{A.4})$$

which can be gained by the fast Fourier transform (FFT).

Finally, the analytical solutions ϕ and ψ can be obtained from Eq. (A.3).

References

- [1] D. Colton and R. Kress, Inverse acoustic and electromagnetic scattering theory, Appl. Math. Sci., 93 (1992).
- [2] G. Bao, H. Y. Liu, P. J. Li and L. Zhang, Inverse obstacle scattering in an unbounded structure, Commun. Comput. Phys., 26 (2019), 1274-1306.
- [3] X. Jiang, Y. Qi and J. H. Yuan, An adaptive finite element PML method for the acoustic scattering problems in layered media, Commun. Comput. Phys., 25 (2019), 266-288.
- [4] X. B. Feng, J. S. Lin and D. P. Nicholls, An efficient monte carlo-transformed field expansion method for electromagnetic wave scattering by random rough surfaces, Commun. Comput. Phys., 23 (2018), 685-705.

- [5] I. Abubakar, Scattering of plane elastic waves at rough surfaces. I, in *Mathematical Proceedings of the Cambridge Philosophical Society*, Cambridge University Press, 58 (1962), 136-157.
- [6] J. Achenbach, *Wave propagation in elastic solids*, Elsevier, 2012.
- [7] I. S. Sokolnikoff and R. D. Specht, *Mathematical theory of elasticity*, New York: McGraw-Hill, 83 (1956).
- [8] L. J. Huang, M. Fehler, Y. Zheng and X. B. Xie, Seismic-wave scattering, imaging, and inversion, *Commun. Comput. Phys.*, 28 (2020), 1-40.
- [9] R. S. Wu, Towards a theoretical background for strong-scattering inversion-direct envelope inversion and Gelfand-Levitan-Marchenko theory, *Commun. Comput. Phys.*, 28 (2020), 41-73.
- [10] X. B. Xie, B. He, H. Ning, Y. He, and B. Chen, The effect of strong near surface scattering on seismic imaging: investigation based on resolution analysis, *Commun. Comput. Phys.*, 28 (2020), 167-186.
- [11] T. Arens, Existence of solution in elastic wave scattering by unbounded rough surfaces, *Math. Methods Appl. Sci.*, 25 (2002), 507-528.
- [12] T. Arens, Uniqueness for elastic wave scattering by rough surfaces, *SIAM J. Math. Anal.*, 33 (2001), 461-476.
- [13] J. J. Bowman, T. B. Senior and P. L. Uslenghi, *Electromagnetic and acoustic scattering by simple shapes (Revised edition)*, in *hpc.*, 1987.
- [14] J. H. Yue, M. Li, P. J. Li and X. K. Yuan, Numerical solution of an inverse obstacle scattering problem for elastic waves via the Helmholtz decomposition, *Commun. Comput. Phys.*, 26 (2019), 809-837.
- [15] J. M. Jin, *The finite element method in electromagnetics*, John Wiley and Sons, 2015.
- [16] F. Ihlenburg, I. Babuska and S. Sauter, Reliability of finite element methods for the numerical computation of waves, *Adv. Eng. Softw.*, 28 (1997), 417-424.
- [17] P. Liu and Y. Q. Jin, Numerical simulation of bistatic scattering from a target at low altitude above rough sea surface under an EM-wave incidence at low grazing angle by using the finite element method, *IEEE Transactions on antennas and propagation*, 52 (2004), 1205-1210.
- [18] D. Colton and R. Kress, *Integral equation methods in scattering theory*, SIAM, 72 (2013).
- [19] Q. H. Ran, X. L. Cheng and S. Abide, A dynamical method for solving the obstacle problem, *Numer. Math. Theor. Meth. Appl.*, 13 (2020), 353-371.
- [20] X. Jiang, P. J. Li and W. Zheng, An adaptive finite element method for the wave scattering with transparent boundary condition, *J. Sci. Comput.*, 72 (2017), 936-956.
- [21] Y. Gao and P. J. Li, Electromagnetic scattering for time-domain Maxwells equations in an unbounded structure, *Math. Methods Appl. Sci.*, 27 (2017), 1843-1870.
- [22] T. Hagstrom, Radiation boundary conditions for the numerical simulation of waves, *Acta numerica.*, 8 (1999), 47-106.
- [23] B. Engquist and A. Majda, Absorbing boundary conditions for numerical simulation of waves, *Pro. National Acade. Sci.*, 74 (1977), 1765-1766.
- [24] M. J. Grote and C. Kirsch, Dirichlet-to-Neumann boundary conditions for multiple scattering problems, *J. Comput. Phys.*, 201 (2004), 630-650.
- [25] J. P. Berenger, A perfectly matched layer for the absorption of electromagnetic waves, *J. Comput. Phys.*, 114 (1994), 185-200.
- [26] X. Jiang and P. J. Li, An adaptive finite element PML method for the acoustic-elastic interaction in three dimensions, *Commun. Comput. Phys.*, 22 (2017), 1486-1507.

- [27] X. Jiang, P. J. Li, J. Lv and W. Zheng, Convergence of the PML solution for elastic wave scattering by biperiodic structures, arXiv preprint arXiv:1611.05717, 2016.
- [28] J. H. Yue, G. R. Liu, M. Li and R. R. Niu, An edge-based smoothed finite element method for wave scattering by an obstacle in elastic media, *Eng. Anal. Bound. Elem.*, 101 (2019), 121-138.
- [29] G. R. Liu, On G space theory, *Int. J. Comput. Methods*, 6 (2009), 257-289.
- [30] G. R. Liu, A G space theory and a weakened weak (W2) form for a unified formulation of compatible and incompatible methods: Part I theory, *Int. J. Numer. Meth. Eng.*, 81 (2010), 1093-1126.
- [31] G. R. Liu and Y. Z. Gui, Smoothed point interpolation methods: G space theory and weakened weak forms, World Scientific, 2013.
- [32] G. R. Liu, T. T. Nguyen, K. Y. Dai and K. Y. Lam, Theoretical aspects of the smoothed finite element method (SFEM), *Int. J. Numer. Meth. Eng.*, 71 (2007), 902-930.
- [33] W. Li, Y. B. Chai, M. Lei and G. R. Liu, Analysis of coupled structural-acoustic problems based on the smoothed finite element method (S-FEM), *Eng. Anal. Bound. Elem.*, 42 (2014), 84-91.
- [34] D. Wan, D. Hu, G. Yang and T. Long, A fully smoothed finite element method for analysis of axisymmetric problems, *Eng. Anal. Bound. Elem.*, 72 (2016), 78-88.
- [35] G. R. Liu and N. Trung, Smoothed finite element methods, CRC press, 2016.
- [36] W. Zeng, and G. R. Liu, Smoothed finite element methods (S-FEM): an overview and recent developments, *Arch. Comput. Methods. Eng.*, 25 (2018), 397-435.
- [37] G. Y. Zhang, Y. Li, X. X. Gao, D. Hui, S.Q. Wang and Z. Zong, Smoothed point interpolation method for elastoplastic analysis, *Int. J. Comput. Methods*, 12 (2015), 1540013.
- [38] G. Wu, J. Zhang, Y. Li, L. Yin and Z. Liu, Analysis of transient thermo-elastic problems using a cell-based smoothed radial point interpolation method, *Int. J. Comput. Methods*, 13 (2016), 1650023.
- [39] S. Z. Feng, X. Y. Cui, F. Chen, S. Z. Liu and D. Y. Meng, An edge/face-based smoothed radial point interpolation method for static analysis of structures, 68 (2016), 1-10.
- [40] Y. Chai, X. You, W. Li, Y. Huang, Z. Yue and M. Wang, Application of the edge-based gradient smoothing technique to acoustic radiation and acoustic scattering from rigid and elastic structures in two dimensions, *Comput. Struct.*, 203 (2018), 43-58.
- [41] W. Li, Y. Chai, M. Lei and T. Li, Numerical investigation of the edge-based gradient smoothing technique for exterior Helmholtz equation in two dimensions, *Comput. Struct.*, 182 (2017), 149-164.
- [42] Y. Chai, W. Li, Z. Gong and T. Li, Hybrid smoothed finite element method for two-dimensional underwater acoustic scattering problems, *Ocean Eng.*, 116 (2016), 129-141.
- [43] W. Li, Y. Chai, M. Lei and G. R. Liu, Analysis of coupled structural-acoustic problems based on the smoothed finite element method (S-FEM), *Eng. Anal. Bound. Elem.*, 42 (2014), 84-91.
- [44] Y. Chai, Z. Gong, W. Li, T. Li and Q. Zhang, A smoothed finite element method for exterior Helmholtz equation in two dimensions, *Eng. Anal. Bound. Elem.*, 84 (2017), 237-252.
- [45] Z. C. He, G. R. Liu, Z. H. Zhang, S. C. Wu, G. Y. Zhang and A. G. Cheng, An edge-based smoothed finite element method (ES-FEM) for analyzing three-dimensional acoustic problems, *Comput. Methods Appl. Mech. Eng.*, 199 (2009), 20-33.
- [46] G. Wang, X. Y. Cui, Z. M. Liang and G. Y. Li, A coupled smoothed finite element method (S-FEM) for structural-acoustic analysis of shells, *Eng. Anal. Bound. Elem.*, 61 (2015), 207-217.
- [47] Y. Li, G. Y. Zhang, G. R. Liu, Y. N. Huang and Z. Zong, A contact analysis approach based on linear complementarity formulation using smoothed finite element methods, *Eng. Anal.*

- Bound. Elem., 37 (2013), 1244-1258.
- [48] J. H. Yue, G. R. Liu, M. Li and R. P. Niu, A cell-based smoothed finite element method for multi-body contact analysis using linear complementarity formulation, *Int. J. Sol. Struct.*, 141 (2018), 110-126.
 - [49] H. Nguyenxuan and G. R. Liu, An edge-based smoothed finite element method softened with a bubble function (bES-FEM) for solid mechanics problems, *Comput. Struct.*, 128 (2013), 14-30.
 - [50] G. R. Liu, T. Nguyenthoi, H. Nguyenxuan and K. Y. Lam, A node-based smoothed finite element method (NS-FEM) for upper bound solutions to solid mechanics problems, *Comput. Struct.*, 87 (2009), 14-26.
 - [51] H. Feng, X. Y. Cui and G. Y. Li, A stable nodal integration method with strain gradient for static and dynamic analysis of solid mechanics, *Eng. Anal. Bound. Elem.*, 62 (2016), 78-92.
 - [52] S. H. Huo, C. Jiang, X. Cui and G. R. Liu, A high-fidelity 3D S-FEM stress analysis of a highly heterogeneous swine skull, *Med. Biol. Eng. Comput.*, 58 (2020), 625-641.
 - [53] Y. Yang, H. Zheng and X. Du, An enriched edge-based smoothed FEM for linear elastic fracture problems, *Int. J. Comput. Methods*, 14 (2017), 1750052.
 - [54] G. R. Liu, L. Chen and M. Li, S-FEM for fracture problems, theory, formulation and application, *Int. J. Comput. Methods*, 11 (2014), 1343003.
 - [55] J. B. Keller and D. Givoli, Exact non-reflecting boundary conditions, *J. Comput. Phys.*, 82 (1989), 172-192.